

Local boundary layer scales in turbulent Rayleigh-Bénard convection

Janet D. Scheel¹ and Jörg Schumacher²

¹Department of Physics, Occidental College, 1600 Campus Road, M21, Los Angeles, California 90041, USA

²Institut für Thermo- und Fluidodynamik, Postfach 100565, Technische Universität Ilmenau, D-98684 Ilmenau, Germany

(Received 2 March 2022)

We compute *fully local boundary layer scales* in three-dimensional turbulent Rayleigh-Bénard convection. These scales are directly connected to the highly intermittent fluctuations of the fluxes of momentum and heat at the isothermal top and bottom walls and are statistically distributed around the corresponding mean thickness scales. The local boundary layer scales also reflect the strong spatial inhomogeneities of both boundary layers due to the large-scale, but complex and intermittent, circulation that builds up in closed convection cells. Similar to turbulent boundary layers, we define *inner scales* based on local shear stress which can be consistently extended to the classical viscous scales in bulk turbulence, e.g. the Kolmogorov scale, and *outer scales* based on slopes at the wall. We discuss the consequences of our generalization, in particular the scaling of our inner and outer boundary layer thicknesses and the resulting shear Reynolds number with respect to Rayleigh number. The mean outer thickness scale for the temperature field is close to the standard definition of a thermal boundary layer thickness. In the case of the velocity field, under certain conditions the outer scale follows a similar scaling as the Prandtl-Blasius type definition with respect to Rayleigh number, but differs quantitatively. The friction coefficient c_ϵ scaling is found to fall right between the laminar and turbulent limits which indicates that the boundary layer exhibits transitional behavior. Additionally, we conduct an analysis of the recently suggested dissipation layer thickness scales versus Rayleigh number and find a transition in the scaling. All our investigations are based on highly accurate spectral element simulations which reproduce gradients and their fluctuations reliably. The study is done for a Prandtl number of $Pr = 0.7$ and for Rayleigh numbers which extend over nearly five orders of magnitude, $3 \times 10^5 \leq Ra \leq 10^{10}$ in cells of aspect ratio of one. We also performed one study of aspect ratio equal to three in the case of $Ra = 10^8$. For both aspect ratios, we find that the scale distributions depend on the position at the plates where the analysis is conducted.

1. Introduction

The key to a deeper understanding of the mechanisms of transport of heat and momentum in turbulent Rayleigh-Bénard convection lies in a better access to the dynamics in the tiny boundary layers of the temperature and velocity fields (Siggia 1994, Ahlers *et al.* 2009, Chillà & Schumacher 2012). The boundary layers (BL) form in the vicinity of the isothermally heated plate at the bottom and the isothermally cooled plate at the top. With increasing Rayleigh number Ra and thus with increasing thermal driving of Rayleigh-Bénard convection, the BL thickness decreases similar to many (isothermal) wall-bounded flows where the BL thickness shrinks with increasing Reynolds number (see e.g. Pope 2000).

The full access to the three-dimensional structure and near-wall dynamics of the BL is still impossible for high-Rayleigh number convection experiments. However in the last few years, successful steps into this direction have been made by monitoring the dynamical evolution in the boundary layer in two-dimensional observation windows using high-resolution particle image velocimetry, such as in Zhou *et al.* (2010), Zhou & Xia (2010), and du Puits *et al.* (2014). Local heat flux measurements on small plate segments such as those by du Puits *et al.* (2010) or Kaiser & du Puits (2014) provide an access to the fluctuating temperature gradient at the walls. Time-averaged local boundary layer profiles were measured by Lui & Xia (1998) for $2 \times 10^8 < Ra < 2 \times 10^{10}$. But for Rayleigh numbers $Ra \gtrsim 10^{12}$, a direct experimental access to the boundary layer is not yet possible (He *et al.* 2012, Urban *et al.* 2012). Only the mean thermal boundary layer thickness can be reproduced from global heat flux measurements. Direct numerical simulations lack the access to this Rayleigh number regime when the aspect ratio of the cell remains larger than or equal to unity (Hartlep *et al.* 2005, Bailon-Cuba *et al.* 2010). Nevertheless, particularly in the last years several direct numerical simulation studies provided new insights into the structure of the boundary layers of both fields, e.g. in van Reeuwijk *et al.* (2008b), Zhou *et al.* (2010), Stevens *et al.* (2010), Stevens *et al.* (2012), Wagner *et al.* (2012), Scheel *et al.* (2012) and Shi *et al.* (2012). The main outcome is that the boundary layers obey a complex three-dimensional dynamics which is strongly time-dependent and coupled to the large-scale circulation in the convection system as well as the small-scale fluctuations in the bulk and the emission of thermal plumes.

The classical definition of a boundary layer thickness is traditionally defined (Ahlers *et al.* (2009); Shi *et al.* (2012)) as the intersection point between the tangent to the time-averaged profile at the plates and the first local maximum of the velocity profile (for δ_v) or the bulk value of the temperature profile (for δ_T). This is known as the slope method. For alternate definitions see Ahlers *et al.* (2009) or Li *et al.* (2012). Note that all standard definitions of boundary layer thickness, such as the displacement thickness, assume the existence of a well-defined mean flow. The thickness of both boundary layers are central quantities in mean field theories for the global heat and momentum transfer (see e.g. Grossmann & Lohse 2000). They are required to divide the dissipation of kinetic energy and thermal variance into bulk and boundary layer dominated volume fractions. The mean thermal boundary layer thickness scales inversely with the Nusselt number Nu , the dimensionless measure of the global heat transfer and is given by

$$\delta_T = \frac{H}{2Nu}, \quad (1.1)$$

with H being the height of the convection layer (or convection cell). The mean boundary layer thickness of the velocity field scales with the square root of the Reynolds number Re and is given by

$$\delta_v = \frac{aH}{\sqrt{Re}}, \quad (1.2)$$

where a is a free parameter which is adjusted to the case of a Prandtl-Blausius type boundary layer (Prandtl 1905, Blasius 1908). There are however applications in nature where these concepts are not applicable, particularly since the derivation relies on no-slip boundary conditions at the isothermal plates at the top and bottom. One such example is the dynamics of the mantle of the Earth where convection models use stress-free boundaries without momentum flux (see e.g. Trompert & Hansen 1998) and for which definition (1.2) does not work. This was one motivation of Petschel *et al.* (2013) to generalize the definition of a boundary layer thickness to that of a *dissipation layer*

thickness (DL). The thickness of the dissipation layer is determined by

$$\langle \epsilon(z = d_v) \rangle_{A,t} = \langle \epsilon \rangle_{V,t} \quad \text{and} \quad \langle \epsilon_T(z = d_T) \rangle_{A,t} = \langle \epsilon_T \rangle_{V,t}. \quad (1.3)$$

Then the smallest distance from a boundary plate to the intersection of these equations defines the DL scales d_v and d_T . Here, ϵ is the rate of kinetic energy dissipation and ϵ_T the thermal dissipation rate (see below for exact definitions). Notations $\langle \cdot \rangle_{A,t}$ and $\langle \cdot \rangle_{V,t}$ denote averages over horizontal planes in combination with time and volume in combination with time, respectively. This definition requires the measurement of profiles of both dissipation rates which is not applicable in experiments. The two methods to calculate thicknesses of boundary layers, either via Eqns. (1.1) and (1.2) or via (1.3), result in mean thickness scales. They do not incorporate the strong spatial inhomogeneities across the isothermal plates. Furthermore, it is well-known from experiments (Lui & Xia (1998), Qiu & Xia (1998), Zhou *et al.* (2010), Zhou & Xia 2010) and simulations (Zhou *et al.* (2011), Wagner *et al.* (2012), Stevens *et al.* (2012), Shi *et al.* 2012) that these thicknesses vary strongly in time and that this is caused by the local detachment of thermal plumes as well as fluctuations in the large-scale circulation and in the bulk.

In this work, we use therefore a *fully local boundary layer scale* definition which incorporates these spatial inhomogeneities. These local boundary layer scales are distributed around a mean scale and thus reflect the strong spatial intermittency of the gradients in the vicinity of the walls in the turbulent convection flow. Our approach is fully local since it is based on gradients evaluated at the plate with spectral accuracy. We define two classes of local boundary layer scales, *inner* and *outer* scales. Our definition for the outer boundary layer scale for the velocity and temperature fields is based on the fluxes of momentum and heat at the wall, respectively. These BL scales are thus length scales which build on an inverse gradient for both fields (excluding zero magnitudes). In addition these local methods can be applied even in the absence of a well-defined mean flow, which is the case in turbulent thermal convection. In the case of the temperature field, the mean of this outer scale is close to Eq. (1.1) which relates the thermal boundary layer thickness to the Nusselt number. In the case of the velocity field, our mean outer scale definition avoids the use of the coefficient a in combination with the prescribed functional dependence on the Reynolds number (see Eq. (1.2.)) This will cause a scaling of the mean velocity boundary layer thickness that is qualitatively similar to that of Eq. (1.2), but differs quantitatively.

The definitions of the inner scales can be consistently related to the local dissipation and diffusion scales which have been developed and investigated for bulk turbulence in several systems (Schumacher *et al.* 2005, Schumacher 2007, Zhou & Xia 2010a, Hamlington *et al.* 2012, Scheel *et al.* 2013). Clearly, velocity gradients in the form of the wall-shear stress enter these definitions again, but now related to molecular viscosity and thermal diffusivity, respectively. Finally, we will compare our analysis with the dissipation layer approach. While in Petschel *et al.* (2013) trends of the dissipation layer thickness with respect to Prandtl number at fixed Rayleigh number are discussed, we investigate the dependence on the Rayleigh number for a Prandtl number of convection in air.

The outline of the manuscript is as follows. In the next section, we will discuss the equations of motion, list essential definitions and describe the numerical method in brief. Results of the mean global transport of heat and momentum are also listed. The third section summarizes the definitions of the local boundary layer scales and relates them to classical equations. The fourth section discusses our results. We present the distributions of the scales and compare the means with classical thickness equations, particularly with respect to the scaling with Rayleigh number. We also compute the resulting shear

Reynolds number and its scaling with Rayleigh number. Furthermore, the spatial averaging is conducted partly locally. Therefore we will analyze scale distributions in different subvolumes, including in an aspect-ratio-of-three cell and compare the findings to a cylindrical cell with aspect ratio one. This analysis is followed by a dissipation layer analysis which we conduct here for varying Rayleigh number. This analysis is followed by a final study of the friction coefficient and compared with existing data from Verzicco & Camussi (2003) and Wei & Xia (2013). We conclude with a final summary and a brief discussion.

2. Methods

We solve the three-dimensional equations of motion in the Boussinesq approximation numerically. The dimensionless form of the equations[†] is based on the height of the cell H , the free-fall velocity $U_f = \sqrt{g\alpha\Delta TH}$ and the imposed temperature difference ΔT . The three control parameters of Rayleigh-Bénard convection are the Rayleigh number Ra , the Prandtl number Pr and the aspect ratio $\Gamma = D/H$ with the diameter D . The resulting equations are:

$$\tilde{\nabla} \cdot \tilde{\mathbf{u}} = 0, \quad (2.1)$$

$$\frac{\partial \tilde{\mathbf{u}}}{\partial \tilde{t}} + (\tilde{\mathbf{u}} \cdot \tilde{\nabla})\tilde{\mathbf{u}} = -\tilde{\nabla}\tilde{p} + \sqrt{\frac{Pr}{Ra}}\tilde{\nabla}^2\tilde{\mathbf{u}} + \tilde{T}\mathbf{e}_z, \quad (2.2)$$

$$\frac{\partial \tilde{T}}{\partial \tilde{t}} + (\tilde{\mathbf{u}} \cdot \tilde{\nabla})\tilde{T} = \frac{1}{\sqrt{RaPr}}\tilde{\nabla}^2\tilde{T}, \quad (2.3)$$

where

$$Ra = \frac{g\alpha\Delta TH^3}{\nu\kappa}, \quad Pr = \frac{\nu}{\kappa}. \quad (2.4)$$

The variable g stands for the acceleration due to gravity, α is thermal expansion coefficient, ν is the kinematic viscosity, and κ is thermal diffusivity. We use aspect ratios of $\Gamma = 1$ and 3. At all walls no-slip boundary conditions for the fluid are applied, i.e., $\mathbf{u} = 0$. The side walls are thermally insulated, i.e., the normal derivative of the temperature field vanishes, $\partial T / \partial \mathbf{n} = 0$. The top and bottom plates are held at constant dimensionless temperatures $\tilde{T} = 0$ and 1, respectively. In response to the input parameters Ra , Pr and Γ , a heat flux is established from the bottom to the top plate. It is determined by the Nusselt number which is defined as

$$Nu(\tilde{z}) = \sqrt{RaPr} \langle \tilde{u}_z \tilde{T} \rangle_{A,t} - \frac{\partial \langle \tilde{T} \rangle_{A,t}}{\partial \tilde{z}}. \quad (2.5)$$

The vertical average of $Nu(\tilde{z})$ results in the volume averaged Nusselt number Nu_V :

$$Nu_V = 1 + \sqrt{RaPr} \langle \tilde{u}_z \tilde{T} \rangle_{V,t}. \quad (2.6)$$

The value Nu_V has to be equal to $Nu(\tilde{z})$ for all $\tilde{z} \in [0, 1]$. The momentum transport is expressed by the Reynolds number which is defined as

$$Re = \sqrt{\frac{Ra}{Pr}} \langle \tilde{\mathbf{u}}^2 \rangle_{V,t}. \quad (2.7)$$

The thermal dissipation rate is given by

$$\tilde{\epsilon}_T(\tilde{\mathbf{x}}, \tilde{t}) = \frac{1}{\sqrt{RaPr}} \left(\frac{\partial \tilde{T}}{\partial \tilde{x}_j} \right)^2, \quad (2.8)$$

[†] Note that all scaled variables will be noted by tildes in this section.

Ra	Γ	N_s	N_e	N	$Nu_v \pm \Delta Nu_v$	$Re \pm \Delta Re$	$\tilde{u}_{rms} \pm \Delta \tilde{u}_{rms}$
$3 \times 10^5*$	1	401	3,520	11	5.80 ± 0.03	116 ± 1	0.177 ± 0.001
$5 \times 10^5*$	1	401	3,520	11	6.90 ± 0.13	151 ± 2	0.179 ± 0.002
$7 \times 10^5*$	1	407	3,520	11	7.78 ± 0.05	179 ± 1	0.180 ± 0.002
1×10^6	1	300	30,720	7	8.65 ± 0.06	214 ± 6	0.179 ± 0.004
5×10^6	1	340	30,720	7	13.79 ± 0.17	483 ± 1	0.181 ± 0.001
1×10^7	1	230	30,720	11	16.77 ± 0.01	675 ± 3	0.179 ± 0.001
5×10^7	1	192	30,720	13	25.8 ± 0.3	1490 ± 40	0.176 ± 0.004
1×10^8	1	87	256,000	11	31.4 ± 1.3	2070 ± 60	0.173 ± 0.005
1×10^8	3	62	2,304,000	9	31.1 ± 0.6	2310 ± 30	0.194 ± 0.002
1×10^9	1	92	875,520	11	63 ± 4	6240 ± 140	0.165 ± 0.004
$1 \times 10^{10*}$	1	41	2,374,400	11	127 ± 6	19300 ± 900	0.161 ± 0.007

TABLE 1. A summary of the parameters used for the convection runs. We list the Rayleigh number Ra , the aspect ratio Γ , the number of statistically independent snapshots N_s , the number of spectral elements N_e , polynomial order N in each space direction and for each element, the Nusselt number Nu_v (see Eq. (2.6)), the Reynolds number Re (see Eq. (2.7)) and the root mean square velocity obtained in the whole cell volume V , i.e. $\tilde{u}_{rms} = \sqrt{\langle \tilde{\mathbf{u}}^2 \rangle_{V,t}}$. All runs are conducted at $Pr = 0.7$. Stars indicate simulations which are new (the rest were first presented in Scheel *et al.* (2013)). The error bars in the last three columns have been obtained by evaluating the results over the first and second halves of the corresponding data set separately and taking the difference of both results subsequently.

and the kinetic energy dissipation rate is defined as

$$\tilde{\epsilon}(\tilde{\mathbf{x}}, \tilde{t}) = \frac{1}{2} \sqrt{\frac{Pr}{Ra}} \left(\frac{\partial \tilde{u}_i}{\partial \tilde{x}_j} + \frac{\partial \tilde{u}_j}{\partial \tilde{x}_i} \right)^2 = 2 \sqrt{\frac{Pr}{Ra}} \tilde{S}_{ij} \tilde{S}_{ji}. \quad (2.9)$$

where \tilde{S}_{ij} is the rate of strain tensor.

The equations are numerically solved by the Nek5000 spectral element method package which has been adapted to our problem. The code employs second order time-stepping, using a second-order backward difference formula. The whole set of equations is transformed into a weak formulation and discretized with the particular choice of spectral basis functions (Fischer 1997, Deville *et al.* 2002). The resulting linear, symmetric Stokes problem is solved implicitly. This system is split, decoupling the viscous and pressure steps into independent symmetric positive definite subproblems which are solved either by Jacobi (viscous) or multilevel Schwartz (pressure) preconditioned conjugate gradient iteration. Fast parallel solvers based on direct projection or more scalable algebraic multigrid are used for the coarse-grid solve that is part of the pressure preconditioner. All derivatives are calculated spectrally when computing the local boundary layer thicknesses in Eqns. (3.3), (3.6) and (3.7). For further numerical details and comprehensive tests of the sufficient spectral resolution, we refer to Scheel *et al.* (2013).

In table 1 we summarize the main parameters of the simulation runs. The total number of mesh cells is calculated by $N_e N^3$ and becomes larger than 4×10^9 for the largest runs. We detect the following power laws for the global transport of heat and momentum. The Reynolds number follows $Re = (0.25 \pm 0.01) \times Ra^{0.49 \pm 0.01}$, the Nusselt number yields $Nu = (0.15 \pm 0.01) \times Ra^{0.29 \pm 0.01}$. Compared to Scheel *et al.* (2013), we extended the series of DNS runs by additional data points at the lower and higher Rayleigh numbers ($3 - 7 \times 10^5$, 5×10^7 , and 1×10^{10} are new) and have run a few time series longer to

improve statistics. We also list the root mean square velocity which is obtained as a combined volume-time average in the whole cell volume V , i.e. $\tilde{u}_{rms} = \sqrt{\langle \tilde{\mathbf{u}}^2 \rangle_{V,t}}$.

3. Local boundary layer scales

3.1. Outer local boundary layer scales

The following definitions are based on the current densities of heat and momentum at the wall, respectively. The heat current density at the plate is purely diffusive and given by

$$J^{\text{heat}}(x, y) = -\kappa \frac{\partial T}{\partial z} \Big|_{z=0}. \quad (3.1)$$

The local temperature slope scale is associated with the inverse (nonzero) gradient and can be defined as

$$\lambda_T^o(x, y) = \frac{\kappa \frac{\Delta T}{2}}{|J^{\text{heat}}(x, y)|} = \frac{H}{2} \left| \frac{\partial \tilde{T}}{\partial \tilde{z}} \right|_{\tilde{z}=0}^{-1}. \quad (3.2)$$

The superscript “o” stands for *outer local boundary layer scale*. The factor $\frac{1}{2}$ is included since the thickness at each of the two isothermal plates is related to one half of the total temperature jump.

Eq. (3.2) is thus a local boundary layer (thickness) scale based on the local slope at each grid point on the plate. It is equivalent to the slope method for an instantaneous local profile, but is much easier to calculate numerically and it is more precise since derivatives are calculated spectrally.

The mean value of this temperature slope scale follows as

$$\langle \tilde{\lambda}_T^o \rangle = \int_0^\infty \tilde{\lambda}_T^o p(\tilde{\lambda}_T^o) d\tilde{\lambda}_T^o = \frac{1}{2} \left\langle \left| \frac{\partial \tilde{T}}{\partial \tilde{z}} \right|_{\tilde{z}=0}^{-1} \right\rangle, \quad (3.3)$$

where $p(\tilde{\lambda}_T^o)$ is the probability density function (PDF) of $\lambda_T^o(x, y)$. It remains to be verified in the simulations if the obtained mean scale coincides with the classical equation of the thermal boundary layer thickness, i.e., $\langle \tilde{\lambda}_T^o \rangle \approx 1/(2Nu) = \tilde{\delta}_T$. Note that it does not follow rigorously (see also Eq.(2.5)).

We proceed in the same way for the velocity field. The momentum current density at the wall has two non-vanishing components and the two-dimensional vector field is given by

$$\mathbf{J}^{\text{mom}}(x, y) = \nu \frac{\partial \mathbf{u}^{(2)}}{\partial z} \Big|_{z=0}, \quad (3.4)$$

with $\mathbf{u}^{(2)} = (u_x, u_y)$. The magnitude of \mathbf{J}^{mom} is the (kinematic) wall shear stress τ_w when an average over plane and time is taken. Two contributions to the local wall shear stress remain in the case of no-slip boundary conditions. In analogy to definition (3.2), we define the local velocity boundary scale

$$\lambda_v^o(x, y) = \frac{\nu u_{rms}}{|\mathbf{J}^{\text{mom}}(x, y)|} = H \tilde{u}_{rms} \left| \frac{\partial \tilde{\mathbf{u}}^{(2)}}{\partial \tilde{z}} \right|_{\tilde{z}=0}^{-1}, \quad (3.5)$$

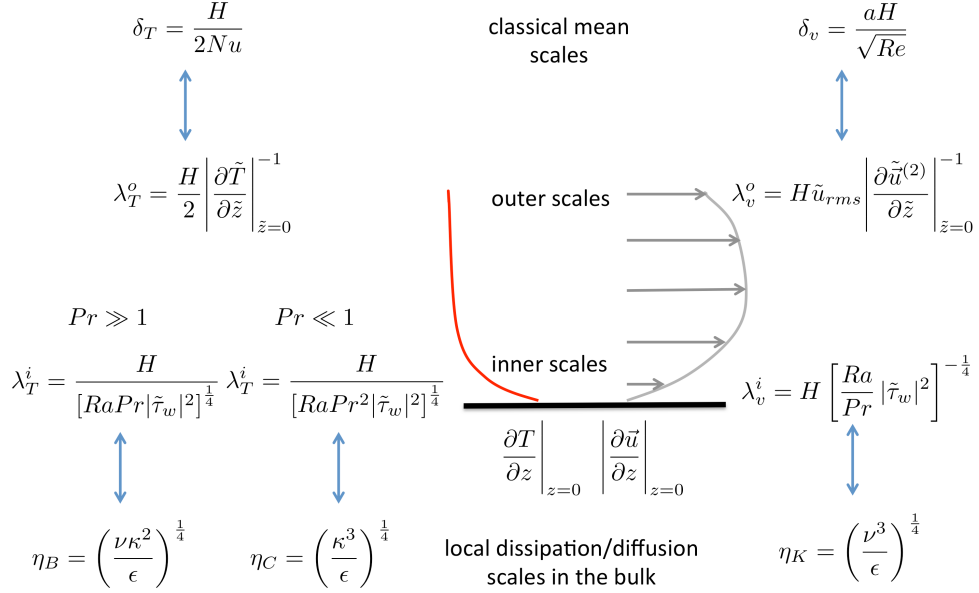


FIGURE 1. A summary diagram of the various connections between the definitions of local boundary layer scales. Similar to turbulent boundary layer theory we suggest outer and inner local scales which can be related to classical mean thickness scales and local dissipation scales in the bulk, respectively. The vertical double-headed arrows indicate the direct connections to other definitions.

and obtain the following mean thickness

$$\langle \tilde{\lambda}_v^o \rangle = \int_0^\infty \tilde{\lambda}_v^o p(\tilde{\lambda}_v^o) d\tilde{\lambda}_v^o = \tilde{u}_{rms} \left\langle \left| \frac{\partial \tilde{u}^{(2)}}{\partial \tilde{z}} \right|_{\tilde{z}=0}^{-1} \right\rangle. \quad (3.6)$$

Eq. (3.6) is again equivalent to the slope method for an instantaneous local profile. However, this definition moves away from the classical thickness equation which incorporates the well-known Reynolds-number dependence of laminar boundary layer theory. Nevertheless we have to introduce a scale factor. In contrast to the temperature scale definition (3.2), where the prefactor of $\frac{1}{2}$ is prescribed by the physical picture of two symmetric boundary layers for the Boussinesq case across which the whole sustained temperature difference drops, it is ab initio undetermined for the velocity. Our prefactor \tilde{u}_{rms} takes therefore the role of the a in the classical equation (1.2) and as this a needs to be determined from experiment (see e.g. Ahlers *et al.* (2009)), our approach will require the evaluation of \tilde{u}_{rms} from simulation. There is a simple geometric picture behind this prefactor. Without any scale factor, we would get a slope scale for the velocity profile which is related to the free-fall velocity U_f . As it has been also discussed in the caption of Table 1 of Bailon-Cuba *et al.* (2010), U_f is more than a factor of 5 bigger than u_{rms} . As a consequence having no scale factor would overestimate our thickness scale. Hence we scale with \tilde{u}_{rms} . We will investigate the relation of our mean scale to the classical Prandtl-Blasius-type equation (1.2) and will test if $\langle \tilde{\lambda}_v^o \rangle \approx a/\sqrt{Re} = \tilde{\delta}_v$ holds. This discussion will follow in subsection 4.2 (see also Tab. 1). The diagram in Fig. 1 displays the connections between the classical thickness scales and our definitions for temperature and velocity.

3.2. Inner local boundary scales

We proceed with the definitions of *inner local boundary scales*. The inner local velocity boundary scale is defined as follows

$$\lambda_v^i(x, y) = \frac{\nu}{\sqrt{|\tau_w(x, y)|}} = \frac{H}{\sqrt{Re_f}} \left[\left(\frac{\partial \tilde{u}_x}{\partial \tilde{z}} \right)^2 + \left(\frac{\partial \tilde{u}_y}{\partial \tilde{z}} \right)^2 \right]_{\tilde{z}=0}^{-\frac{1}{4}}, \quad (3.7)$$

where $Re_f = \sqrt{Ra/Pr}$ is a Reynolds number based on cell height H and free-fall velocity U_f . The definition corresponds to the well-known inner scale from turbulent boundary layer theory, $\lambda_+ = \nu/u_\tau$ with the (mean) friction velocity u_τ (see e.g. Pope 2000). One obtains the following mean thickness

$$\langle \tilde{\lambda}_v^i \rangle = \int_0^\infty \tilde{\lambda}_v^i p(\tilde{\lambda}_v^i) d\tilde{\lambda}_v^i = \left(\frac{Pr}{Ra} \right)^{\frac{1}{4}} \langle |\tilde{\tau}_w|^{-\frac{1}{2}} \rangle. \quad (3.8)$$

Here and in Fig. 1, we abbreviated $|\tilde{\tau}_w| = ((\partial_{\tilde{z}} \tilde{u}_x)^2 + (\partial_{\tilde{z}} \tilde{u}_y)^2)^{1/2}_{\tilde{z}=0}$. The inner local velocity boundary layer scale is related to the local dissipation scale which has been defined in Schumacher *et al.* (2005) or Scheel *et al.* (2013). In this framework, the (mean) Kolmogorov scale $\eta_K = \nu^{3/4}/\langle \epsilon \rangle^{1/4}$ was generalized to a local dissipation scale

$$\tilde{\eta}_K(\tilde{\mathbf{x}}, \tilde{t}) = \left(\frac{Pr}{Ra} \right)^{\frac{3}{8}} \tilde{\epsilon}(\tilde{\mathbf{x}}, \tilde{t})^{-\frac{1}{4}}. \quad (3.9)$$

When applying definition (2.9) and defining a local shear rate on the basis of the rate of strain tensor

$$\tilde{S}(\tilde{\mathbf{x}}) = \sqrt{\tilde{S}_{ij} \tilde{S}_{ji}}, \quad (3.10)$$

one ends up with a consistent translation into our definition of the local inner velocity boundary thickness $\tilde{\lambda}_v^i(\tilde{x}, \tilde{y})$

$$\begin{aligned} \lim_{\tilde{z} \rightarrow 0} \tilde{\eta}_K(\tilde{\mathbf{x}}, \tilde{t}) &= \left(\frac{Pr}{Ra} \right)^{\frac{1}{4}} \lim_{\tilde{z} \rightarrow 0} \left[\sqrt{2} \tilde{S}(\tilde{\mathbf{x}}, \tilde{t}) \right]^{-\frac{1}{2}} \\ &= \left(\frac{Pr}{Ra} \right)^{\frac{1}{4}} \left[\frac{1}{2} \left(\frac{\partial \tilde{u}_x}{\partial \tilde{z}} \right)^2 + \frac{1}{2} \left(\frac{\partial \tilde{u}_y}{\partial \tilde{z}} \right)^2 \right]_{\tilde{z}=0}^{-\frac{1}{4}} = \sqrt[4]{2} \tilde{\lambda}_v^i(\tilde{x}, \tilde{y}). \end{aligned} \quad (3.11)$$

Since the fourth root of 2 is close to unity, both scales practically coincide when approaching the boundary from the bulk. Thus, the analysis which has been formerly conducted in the bulk of the convection cell (see Scheel *et al.* (2013)) can be systematically continued to the walls at the heating and cooling plates.

In the case of the temperature field, we will have to distinguish between small and large Prandtl numbers. The inner scale of temperature field can then be obtained in a similar way to how the Corrsin and Batchelor diffusion scales are obtained in the regimes of low- and high-Prandtl-number convection, respectively (see e.g. Grötzbach 1983, Schumacher *et al.* 2005). The (mean) Corrsin scale is given by $\eta_C = \kappa^{3/4}/\langle \epsilon \rangle^{1/4} = \eta_K/Pr^{3/4}$ and the (mean) Batchelor scale $\eta_B = \kappa^{1/2}\nu^{1/4}/\langle \epsilon \rangle^{1/4} = \eta_K/\sqrt{Pr}$, respectively. Consequently, we can define the following local scales

$$\tilde{\lambda}_T^i(\tilde{x}, \tilde{y}) = \frac{\tilde{\lambda}_v^i(\tilde{x}, \tilde{y})}{\sqrt{Pr}} = (RaPr)^{-\frac{1}{4}} \left[\left(\frac{\partial \tilde{u}_x}{\partial \tilde{z}} \right)^2 + \left(\frac{\partial \tilde{u}_y}{\partial \tilde{z}} \right)^2 \right]_{\tilde{z}=0}^{-\frac{1}{4}} \quad \text{for } Pr \geq 1, \quad (3.12)$$

and

$$\tilde{\lambda}_T^i(\tilde{x}, \tilde{y}) = \frac{\tilde{\lambda}_v^i(\tilde{x}, \tilde{y})}{Pr^{\frac{3}{4}}} = (RaPr^2)^{-\frac{1}{4}} \left[\left(\frac{\partial \tilde{u}_x}{\partial \tilde{z}} \right)^2 + \left(\frac{\partial \tilde{u}_y}{\partial \tilde{z}} \right)^2 \right]_{\tilde{z}=0}^{-\frac{1}{4}} \quad \text{for } Pr \leq 1. \quad (3.13)$$

Since the inner boundary scales for temperature differ only by powers of Ra and Pr compared to λ_v^i , the distributions will just be shifted with respect of those of λ_v^i (see e.g. Schumacher *et al.* (2005)). Therefore we will only calculate the inner local velocity scale λ_v^i in this paper.

We refer once more to Fig. 1 where our definitions are summarized. All the local scale definitions require us to exclude the zero-gradient points. In the case of the temperature field, zero gradients at the walls are excluded a priori due to solely diffusive transport. We have verified this in our data sets. In the case of the velocity boundary layer zero-gradient events remain at and below 1% of all events. The number is found to decrease with increasing Rayleigh number. These local events are avoided only when averages over an ensemble or over an area in combination with time are taken as in the definitions of mean thickness scales. We will come back to this point at the end of subsection 4.5.

From now on, we will use the dimensionless quantities only and drop the tildes in all expressions for convenience.

4. Results

4.1. Distribution of local boundary layer scales across the boundary plates

The strong variation of the local boundary layer scales becomes clearly visible in Fig. 2 where we display contours of instantaneous plots of $\lambda_T^o(x, y)$ and $\lambda_v^i(x, y)$. For comparison, we add the temperature and velocity fields to the figure from which the boundary layer scales have been derived. One sees that the local boundary layer scale of the temperature field (upper left) is well-correlated with the original temperature (lower left). Local maxima of T which indicate local detachments of thermal plumes are in line with enhanced local thicknesses. Likewise the right column of Fig. 2 shows the results of using equation (3.5) for the local inner velocity boundary layer scale (upper right) for the bottom plate. One sees that this boundary layer scale is anticorrelated with the magnitude of the horizontal velocity (lower right). The explanation for this behavior can be given based on the boundary conditions. Large horizontal velocities in the vicinity of the no-slip bottom boundary plane generate steep transversal velocity derivatives which cause a small inverse slope scale.

Next, we plot the unscaled results of the probability density functions (PDFs) for representative Rayleigh numbers in the left column of Fig. 3. These data are taken over the entire bottom and top plates and over a sequence of snapshots. Note the steady march towards smaller values of the BL thickness as the Rayleigh number increases. We will investigate the scaling laws for the mean values of these distributions further below. Note also the fairly wide distribution in boundary layer thicknesses about the mean, which is consistent with what was found by Lui & Xia (1998). In the right column Fig. 3 we replot the PDFs, now scaled with their respective mean values as given in (3.3), (3.6), and (3.8). We denote the mean of the PDF obtained for the whole cross section planes of the cylindrical cell, A , by $\langle \cdot \rangle_A$. Note the overall universal behavior and good collapse for both the local boundary layer scales of velocity and temperature over most of the range. The PDFs always deviate from a lognormal distribution which would be perfectly symmetric with respect to $\lambda/\langle \lambda \rangle = 1$ in a double-logarithmic plot. However λ_v^o does not collapse as well as λ_T^o or λ_v^i .

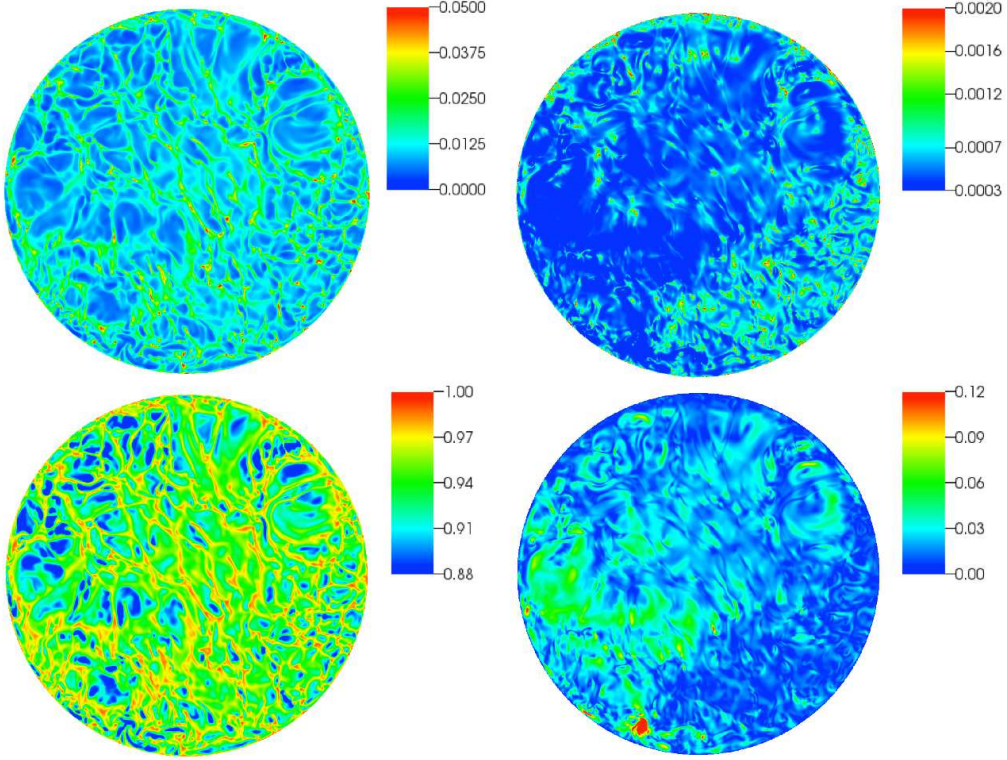


FIGURE 2. Contour plots of snapshots of the local boundary layer scales and original turbulent fields. Top row: Snapshots of the outer local thermal boundary layer scale λ_T^o (left) and the local inner velocity boundary layer thickness λ_v^i (right). Both plots are taken at the bottom plate. Bottom row: Snapshots of temperature T (left) and the velocity magnitude (right). Both contour plots are taken at $z = 0.0005$ for $Ra = 10^{10}$, $\Gamma = 1.0$ and $Pr = 0.7$. All thickness scales are measured in units of H .

The lower left plot in Fig. 3 deserves more comment, as one can clearly observe unphysical local outer velocity boundary layer thicknesses that are larger than H . This is a consequence of very shallow vertical gradients in $\mathbf{u}^{(2)}$ that can occur locally which lead to very large values of $\langle \lambda_v^o \rangle$. The multiplication by u_{rms} in our definition (3.6) helps mitigate these shallow gradients, but still does not eliminate them. We have chosen to present the data as is, since locally these data still do correctly quantify the local boundary layer thickness right at the plate, and do not wish to impose additional prefactors or cutoff values.

We further investigate the local BL thickness PDFs by restricting our analysis to the “bulk” of the plates, where the bulk is defined as all of those BL thickness quantities computed for radii $r < 0.3$. This removes the sidewall effects. It is well-known (Lui & Xia (1998), Stevens *et al.* (2010), Wagner *et al.* (2012)) that the boundary layer thicknesses differ between the center of the plate and the sidewalls because of the backrolls and jets at the sidewalls. Our results here support this. The first moment of the PDF obtained from these data is denoted as $\langle \cdot \rangle_b$. We show these PDFs as a function of the Rayleigh number scaled with the corresponding mean value in the right column of Fig. 4. We normalize our bulk PDFs with the corresponding reduced plate area. Note that the PDFs taken over the entire plate (as shown in the left column) span a wider range of boundary layer thicknesses than their corresponding bulk PDFs. Also for the PDFs taken over the whole

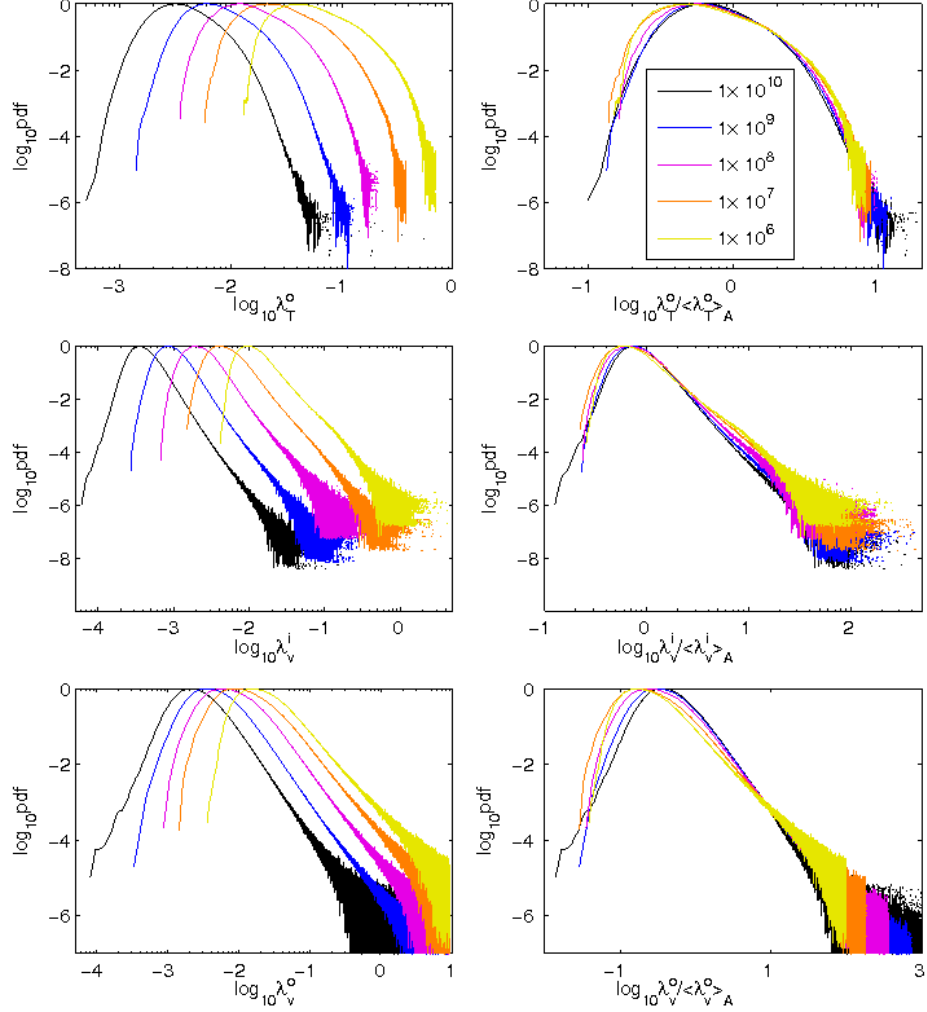


FIGURE 3. Probability density functions (PDFs) of the outer local thermal boundary layer scale (top), the local inner velocity boundary layer thickness (middle) and the local outer velocity boundary layer thickness (bottom) for $\Gamma = 1.0$ and $Pr = 0.7$. The range of Rayleigh numbers is given in the legend. Data are obtained over a sequence of snapshots and the whole bottom and top plates. All thickness scales are measured in units of H .

plate there is a consistent trend towards smaller scales in the right tails as Rayleigh number increases. In contrast, for the PDFs taken over the bulk, the overall collapse is excellent.

To better understand the collapse of the data, we compare scaling of the x -axis of the PDFs with the mean value as computed from (3.3) in the lower plot of Fig. 5 with the mean value computed from the theoretical value for δ_T (see Eq. (1.1)) in the upper plot. Note the data collapse better for the scaling with the mean value of the PDF. However, the collapse is still good for the scaling with the theoretical value, except for a stronger trend towards smaller scales in the right tail for the largest Rayleigh numbers. The good

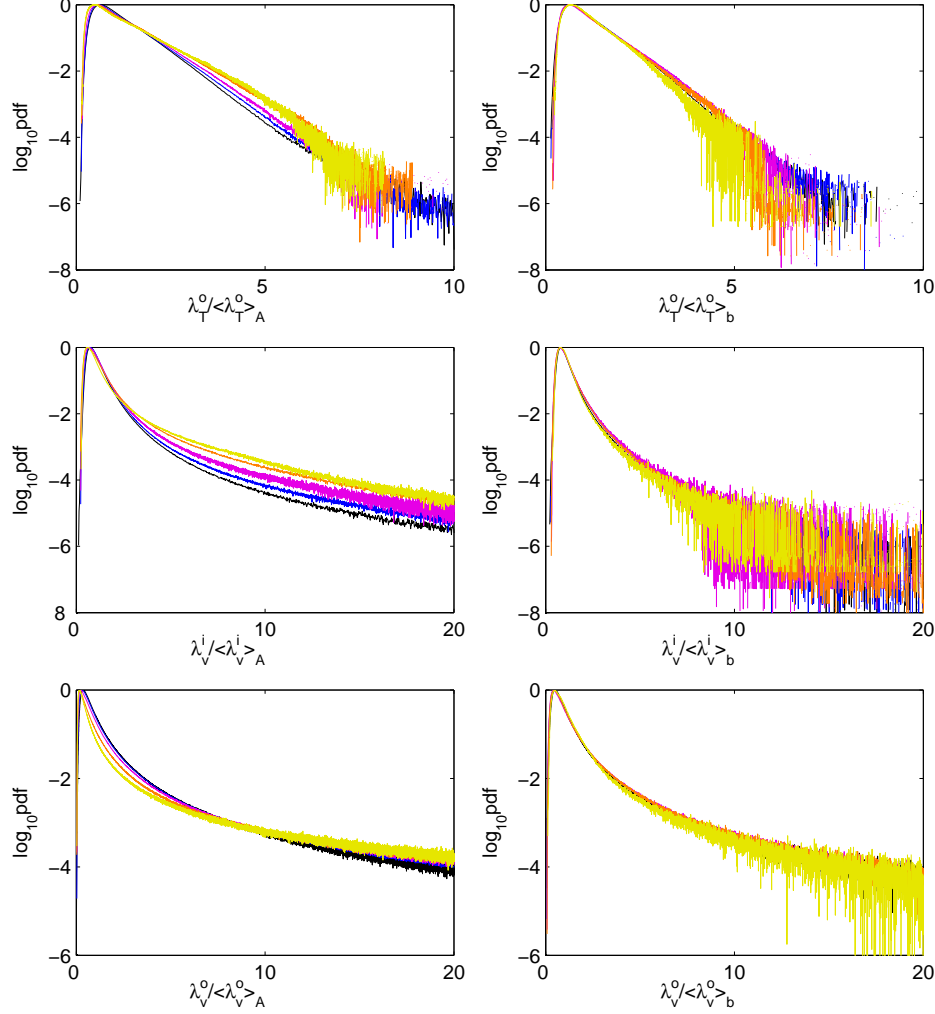


FIGURE 4. PDFs of the local thermal boundary layer thickness (top row), the local inner velocity boundary layer thickness (middle) and the local outer velocity boundary layer thickness (bottom) for $\Gamma = 1.0$ and $Pr = 0.7$. The range of Rayleigh number is the same as in Figure 3. In this case, each PDF is scaled by its mean value. The left column shows the same data as in the right column of Figure 3 (but on a semilogarithmic plot now) and the right column shows the PDF results taken over a “bulk” region defined as radius $r < 0.3$, but still averaged over the bottom and top plates as well as the time.

collapse of the data suggests that our generalization to the outer local boundary layer scale of the temperature can be related consistently to the classical thermal boundary layer thickness Eq. (1.1), i.e., $\langle \lambda_T^o \rangle \sim \delta_T$. In Fig. 6 we compare the collapse of the data for the local boundary layer scales of velocity. In the case of the inner scales, $\lambda_v^i(x, y)$, we see once more a good collapse in the center of the PDF when amplitudes are normalized by $\langle \lambda_v^i \rangle$. As expected the collapse is not obtained when the inner scales are normalized by the Prandtl-Blasius type expression for δ_v found from Eq. (1.2). As can be seen in the

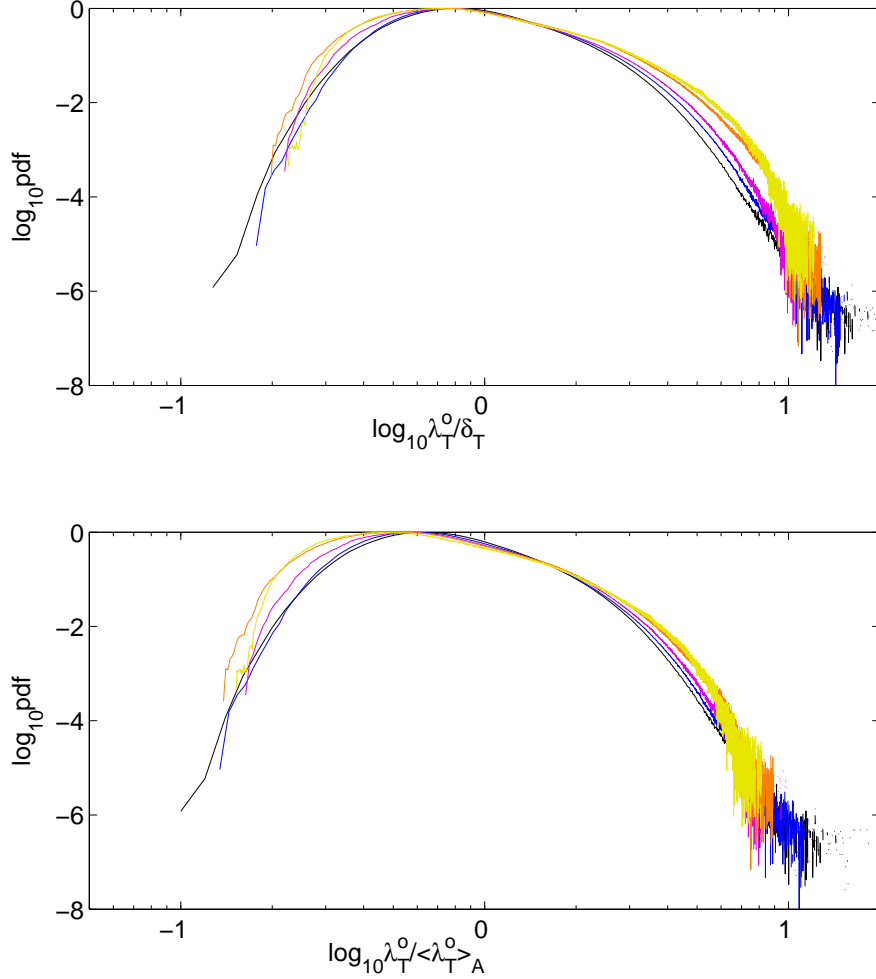


FIGURE 5. PDFs of the local thermal boundary layer thickness where the mean value is obtained from (top) the Nusselt number (as listed in Tab. 1) and given by Eq. (1.1) or (bottom) the average of the PDF as given by Eq. (3.3) for $\Gamma = 1.0$ and $Pr = 0.7$. The range of Rayleigh numbers is the same as in Figure 3. The data collapses better when scaled by the average of the PDF. Both analyses have been carried out with respect to the whole cross sections at top and bottom.

lower left panel of the figure, the opposite is the case for the outer slope-based scale. The data collapses now quite well for a rescaling by both, δ_v and $\langle \lambda_v^o \rangle$. The data also show that the collapse of the distributions is significantly better for δ_v . The coefficient in Eq. (1.2) was taken to $a = 1/4$ following Ahlers *et al.* (2009). To conclude, the mean outer scale can be consistently related to the classical equation, i.e. $\langle \lambda_v^o \rangle \sim \delta_v$. Qualitatively, both scales display thus the same trend with Rayleigh number.

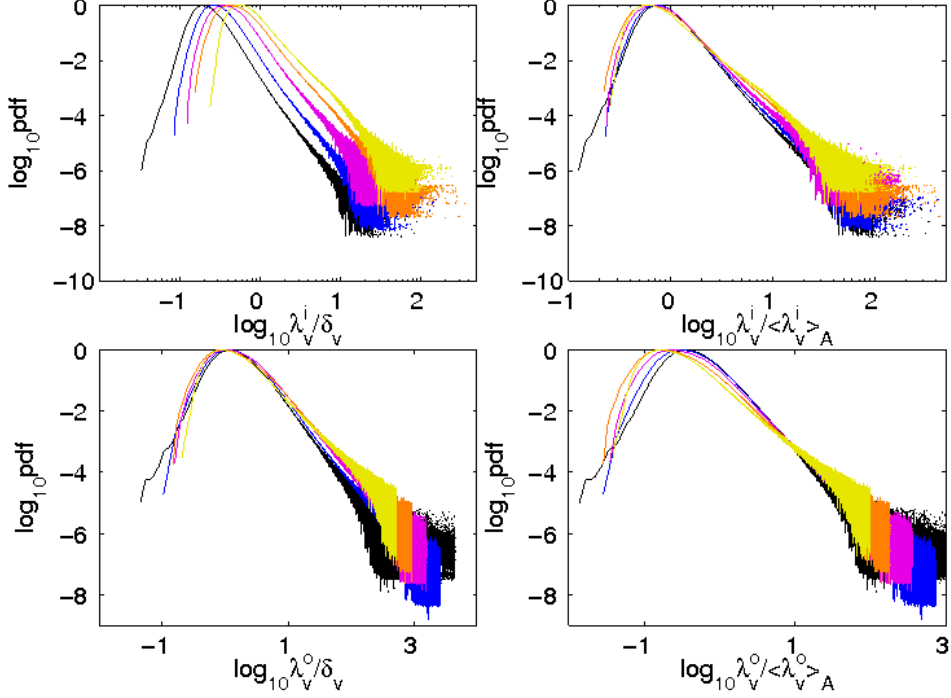


FIGURE 6. PDFs of the inner (top) and outer local velocity boundary layer scale (bottom) where the mean value is obtained from (left column) the Reynolds number as listed in Tab. 1 and given by Eq. (1.2) or (right column) the average of the PDF as given by Eq. (3.6) for $\Gamma = 1.0$ and $Pr = 0.7$. The range of Rayleigh numbers is the same as in Figure 3. Both analyses have been carried out with respect to the whole cross sections at top and bottom.

4.2. Scaling of mean thickness scales with Rayleigh number

In the following we investigate the scaling laws for the mean boundary layer thickness scales with respect to Rayleigh number. Relations (3.3), (3.6) and (3.8) are applied. Representative plots of the location of the mean boundary layer thickness scales in relation to the mean temperature (left column) and mean velocity profiles (right column) are shown in Fig. 7. For the velocity profiles, we used

$$u_{rms,k}^{(2)}(z) = \sqrt{\langle u_x^2 + u_y^2 \rangle_{k,t}} \quad (4.1)$$

where $k = \{A, b\}$. Vertical lines are drawn to highlight the location of the various boundary layer thicknesses. In the upper left plot, we show $\langle \lambda_T^o \rangle_A$ (dashed-dotted line) and δ_T (dotted line). We also plot δ_T^{sl} (dashed line), which is the boundary layer thickness found from the slope method for the plotted profile. Note that our calculated $\langle \lambda_T^o \rangle_A$ lies further from δ_T than the value obtained from δ_T^{sl} . Similar vertical lines are plotted in the top right panel for the velocity boundary layer thicknesses along with $\langle \lambda_v^i \rangle_A$ (solid vertical line). One sees that the outer thickness scales are larger than the (appropriately named) inner thickness scales, and also that δ_v obtained from Eq. (1.2) falls in between, as does δ_v^{sl} . We see that again δ_v^{sl} agrees better with δ_v than our calculated $\langle \lambda_v^o \rangle_A$. The bottom panels show that the bulk-averaged profiles (solid gray curved lines) rise more steeply than the profiles obtained from averaging over the entire area (solid black curved lines).

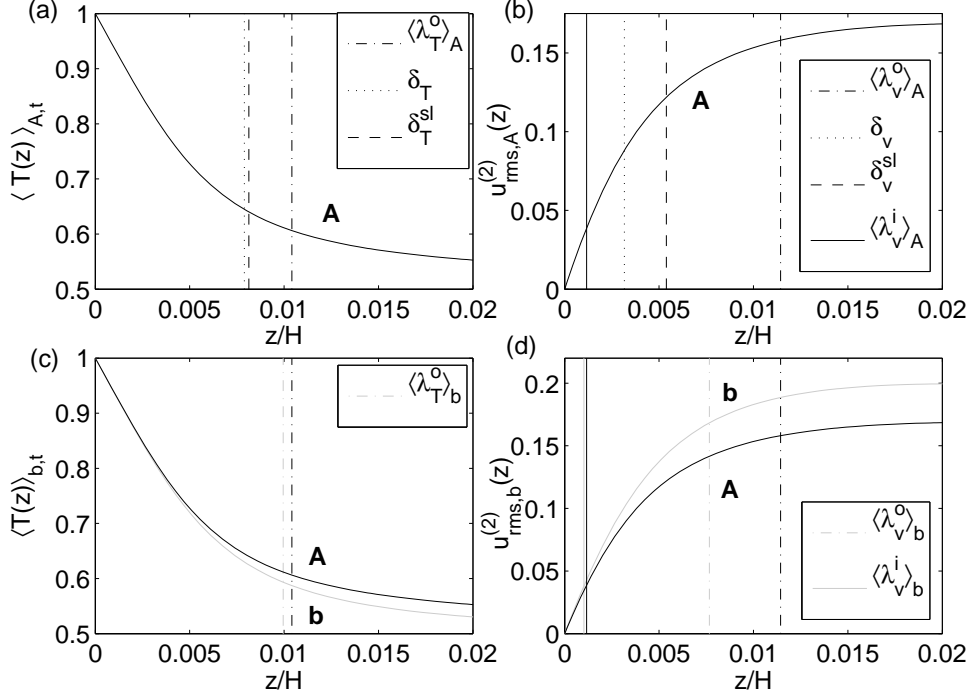


FIGURE 7. A representative illustration of the mean boundary layer thickness scales for a Rayleigh number of 1×10^9 . (a) Plot of the time-averaged temperature profile averaged over the whole plate ($\langle T(z) \rangle_{A,t}$ (solid line)). The vertical lines indicate the location of the computed mean boundary layer thicknesses: the dashed-dotted line corresponds to $\langle \lambda_T^o \rangle_A$, the dotted line corresponds to δ_T , and the dashed line corresponds to δ_T^{sl} . (b) Plots of the time averaged profile $u_{rms,A}^{(2)}(z)$ as defined in Eq. (4.1) (see solid line). The vertical lines now correspond to: $\langle \lambda_v^o \rangle_A$ (dashed-dotted line), $\langle \lambda_v^i \rangle_A$ (solid vertical line), δ_v (dotted line) and δ_v^{sl} (dashed line). Panels (c) and (d) show some of the same data as the upper plots. All of the black lines are the same as in the corresponding panels (a) and (b), but the lighter gray lines indicate bulk-averaged quantities ($r < 0.3$) instead.

This is why we tend to obtain smaller bulk-averaged boundary layer thicknesses (vertical gray lines), which are shown on the plots along with the corresponding area-averaged quantities (vertical black lines). Whereas for the thermal boundary layer thicknesses, all values are quite close to one another, the bulk-averaged quantity $\langle \lambda_v^o \rangle_b$ agrees better with δ_v than the plate-averaged outer boundary layer thickness $\langle \lambda_v^o \rangle_A$. We chose to plot the raw data to highlight the steeper rise and correspondingly smaller boundary layer thicknesses for the bulk-averaged quantities.

The scaling results are summarized in Fig. 8 for the temperature and in Fig. 9 for the velocity. The corresponding classical values for the BL thicknesses are given by (1.1) and (1.2), respectively. Again, we took $a = 1/4$ for δ_v .

The agreement in Fig. 8 between $\langle \lambda_T^o \rangle_A$ and $\langle \lambda_T^o \rangle_b$ is fairly good, especially for larger Rayleigh numbers. We conjecture that this convergence is caused by the increasing filamentation of the thermal plumes as the Rayleigh number grows. As a larger number of finer plumes are distributed across the plane, the side wall regions become increasingly less important. Consequently, the results obtained for planes A and b converge.

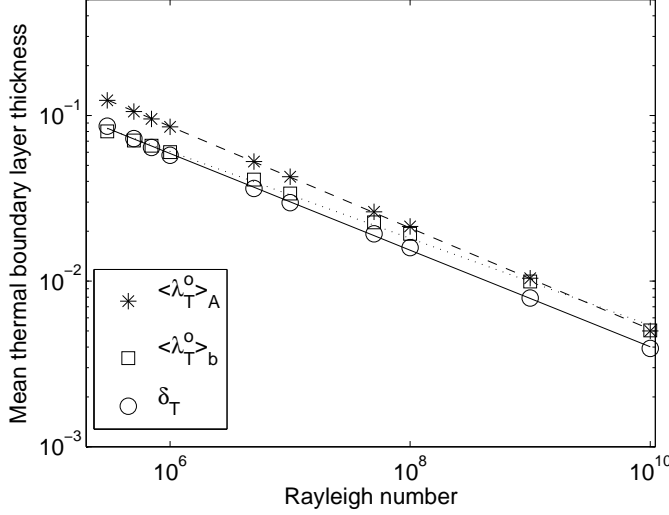


FIGURE 8. Scaling of mean thermal boundary layer thickness with Rayleigh number for different analysis methods. The asterisks are for $\langle \lambda_T^o \rangle_A$ taken over the whole cell and with respect to time, and the fit is $\langle \lambda_T^o \rangle_A = (5.9 \pm 0.2) Ra^{-0.31 \pm 0.01}$ (dashed line). The open squares are for $\langle \lambda_T^o \rangle_b$ taken over the bulk volume with $r < 0.3$, and the fit is $\langle \lambda_T^o \rangle_b = (2.3 \pm 0.3) Ra^{-0.26 \pm 0.01}$ (dotted line). The open circles are the theoretical values for δ_T as defined in Eq. (1.1) with the Nusselt numbers taken from Tab. 1 and the fit is $\delta_T = (3.3 \pm 0.3) Ra^{-0.29 \pm 0.01}$ (solid line).

Conversely for the lower Rayleigh numbers, the large-scale circulation and corresponding sidewall backrolls and jets are comparatively stronger so one expects a larger difference between planes A and b . The classical boundary layer thickness scaling is always a bit lower than our mean local boundary layer thicknesses, with a larger discrepancy at lower Rayleigh number and when averaging over A instead of b . We find that the steep vertical gradients of the temperature field at the plate (the pdf of dT/dz is highly skewed towards larger magnitudes) cause a larger Nu and hence smaller δ_T . Whereas when performing the average in (3.3), the inverse of those steep gradients make very little contribution to $\langle \lambda_T^o \rangle$ and hence our mean local boundary layer thicknesses tend to be on average a bit larger. This effect is enhanced when averaging over A instead of b .

The analysis for the velocity in Fig. 9 deserves a closer inspection. First, the outer scales over the whole plane A or the bulk b are larger than the classical thickness scales δ_v as was also seen in Fig. 7. This indicates some freedom which is always left in the definitions due to different possible choices of the velocity. Interestingly, the scaling exponent of $\langle \lambda_v^o \rangle_A$ agrees better with δ_T than δ_v which suggests that performing an average over the entire plate for the velocity BL thickness is problematic. Second, the mean scales averaged across the whole plane are significantly larger than the mean scales averaged across the bulk, especially for lower Rayleigh numbers. Third, the mean bulk scales $\langle \lambda_v^o \rangle_b$ decrease slower than the mean scales across the whole plane, $\langle \lambda_v^o \rangle_A$. We conclude that the recirculation processes close to the sidewalls which enhance the local boundary layer thickness become increasingly less dominant. As a consequence, a convergence of both sets of scales is observed, similar to the outer local thermal boundary scales, $\langle \lambda_T^o \rangle_A$ and $\langle \lambda_T^o \rangle_b$. Our finding of a thicker local boundary scale close to the side walls is consistent with the result obtained by Lui & Xia (1998) and Wagner *et al.* (2012) (see e.g. their Fig. 19). It is clear that these effects become more pronounced for smaller aspect ratio cells, and suggests that any BL analysis for $Ra < 10^{10}$ needs to carefully consider where

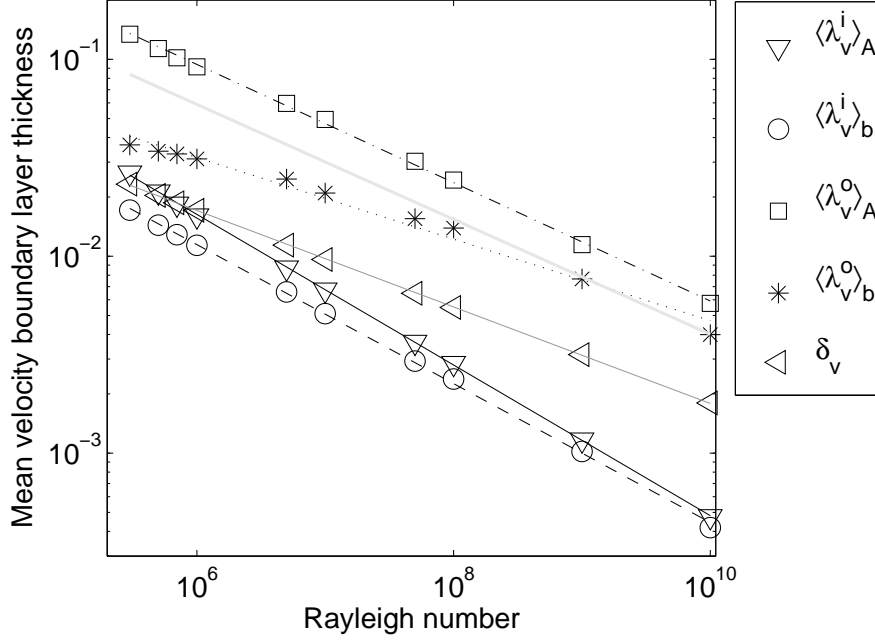


FIGURE 9. Scaling of mean velocity boundary layer thickness with Rayleigh number for different analysis methods. The open downward directed triangles are for $\langle \lambda_v^i \rangle_A$ taken over the whole cell, and the fit is $\langle \lambda_v^i \rangle_A = (3.2 \pm 0.2) Ra^{-0.38 \pm 0.01}$ (solid black line). The open circles are for $\langle \lambda_v^i \rangle_b$ taken over the bulk, and the fit is $\langle \lambda_v^i \rangle_b = (1.5 \pm 0.2) Ra^{-0.35 \pm 0.01}$ (dashed black line). The open squares are for $\langle \lambda_v^o \rangle_A$ taken over the whole cell, and the fit is $\langle \lambda_v^o \rangle_A = (5.9 \pm 0.7) Ra^{-0.30 \pm 0.01}$ (dash-dotted black line). The asterisks are for $\langle \lambda_v^o \rangle_b$ taken over the bulk, and the fit is $\langle \lambda_v^o \rangle_b = (0.55 \pm 0.18) Ra^{-0.21 \pm 0.01}$ (black dotted line). Note that the fit to the last six data points is $\langle \lambda_v^o \rangle_b = (1.0 \pm 0.4) Ra^{-0.24 \pm 0.01}$. The leftward pointing open triangles are the theoretical values for δ_v as defined in Eq. (1.2) with the Reynolds numbers taken from Tab. 1 and $a = 1/4$. The fit is $\delta_v = (0.50 \pm 0.02) Ra^{-0.25 \pm 0.01}$ (gray solid line). For comparison, we also added the fit for δ_T taken from Fig. 8 as a solid bright gray line without symbols.

to perform averages over the plates. We finally note that the inner scales for the velocity field yield consistently significantly smaller values than δ_v .

We compare our scaling results with previous published results in Table 2, where the coefficients are given by

$$\delta_T = \alpha_T Ra^{\beta_T} \quad \delta_v = \alpha_v Ra^{\beta_v} \quad (4.2)$$

Since the coefficients tend to be sensitive to the particular parameters (Ra, Pr, Γ) we only selected experiments and numerical simulations which most closely resembled the current analysis. We also selected to compare only our coefficients for the scaling of the outer thicknesses. This most closely agrees with the slope method which was used in the other works. Since the spatial averaging in most of the other works either was local or removed the sidewall area (except for Verzicco & Camussi (1999)), we also chose to use our bulk averaged values. We find that the overall agreement in the table for the exponents β is fairly good. If we use only the last six data points ($Ra \geq 1 \times 10^7$) for the fit to $\langle \lambda_v^o \rangle_b$ in Fig. 9 we obtain $\langle \lambda_v^o \rangle_b = (1.0 \pm 0.4) Ra^{-0.24 \pm 0.01}$, which gives even better agreement with the other works in Table 2. We find that the agreement with the coefficients α is not as satisfactory. The disagreement for both α and β may in part be

Group	Range of Ra	α_T	β_T	α_v	β_v
Current work*	$10^5 - 10^{10}$	2.3 ± 0.3	-0.26 ± 0.01	0.55 ± 0.18	-0.21 ± 0.01
Scheel <i>et al.</i> (2012)*	$10^5 - 10^8$	1.76 ± 0.12	-0.25 ± 0.01	0.40 ± 0.14	-0.18 ± 0.01
Li <i>et al.</i> (2012)	$10^9 - 10^{12}$	0.42	-0.24	0.90	-0.24
Wagner <i>et al.</i> (2012)*	$10^4 - 10^9$	(—)	-0.285 ± 0.003	(—)	-0.238 ± 0.009
du Puits <i>et al.</i> (2007b)	$10^9 - 10^{12}$	(—)	-0.2540	(—)	(—)
Verzicco & Camussi (1999)*	$10^5 - 10^8$	3.1	-0.29	0.95	-0.23
Belmonte <i>et al.</i> (1994)	$10^7 - 10^{11}$	2.5	-0.29	(—)	(—)

TABLE 2. Comparison of scaling coefficients for the thermal and velocity boundary layer thicknesses (see Eq. (4.2))

. For the current work we selected the scaling for $\langle \lambda_T^o \rangle_b$ and likewise $\langle \lambda_v^o \rangle_b$ since these most closely resemble the methods used in the rest of the referenced works. We only selected cases for $Pr \simeq 0.7$, $\Gamma \simeq 1$ and the Rayleigh number range (given) which overlapped with our data range. The asterisks indicate numerical simulations; the others are experiments.

explained by the subtle differences in the extraction of boundary layer thicknesses for all of the compared cases and suggests that the coefficients (especially α) are much more sensitive to the details of the measurements. Differences could also be attributed to the slightly different Rayleigh number ranges used.

What are the consequences of our mean thickness scales for the scaling of the shear Reynolds number Re_s with respect to the Rayleigh number Ra ? We define the shear Reynolds numbers for the whole cell and the bulk as

$$Re_{s,k} = \sqrt{\frac{Ra}{Pr}} \left[u_{rms,k}^{(2)}(z) \Big|_{z=\langle \lambda_v^o \rangle_k} \langle \lambda_v^o \rangle_k \right], \quad (4.3)$$

where $u_{rms,k}^{(2)}(z)$ is given by Eq. (4.1) and $k = \{A, b\}$. Figure 10 displays the shear Reynolds numbers as a function of the Rayleigh number and the corresponding fits which have been obtained for the six largest Rayleigh numbers in each of the two data sets. We note that the scaling exponent of the mean thickness obtained for the bulk b is larger than the one for the whole area A which underlines the substantial influence of the side wall regions, even for an aspect ratio $\Gamma = 1$. Averaging over the entire plate continues to be problematic here, just as in Fig. 9. Our bulk-averaged data agrees with Li *et al.* (2012) ($Re_s \propto Ra^{0.267 \pm 0.0386}$) who determined the average by profile measurements at centerline of the cell. However, our scaling exponents are smaller and prefactors larger than those obtained by Wagner *et al.* (2012) ($Re_s = 0.072 Ra^{0.2675}$), who also used a local (slope) method and a bulk average, but used the most probable boundary layer thickness instead of the mean value as in Eq. (3.6). The most probable boundary layer thickness is smaller in all cases (see Figure 3) than the first moment, which may explain the difference in coefficients. Our Rayleigh number range is also higher by a factor of 10, which could also account for the differences.

The line of thought we followed here is to obtain the mean thickness as a mean of local slope scales and to combine this with a mean horizontal velocity at a distance from the wall which is exactly given by this mean. This gives us a shear Reynolds number in such a way that no free parameter is left in our analysis.

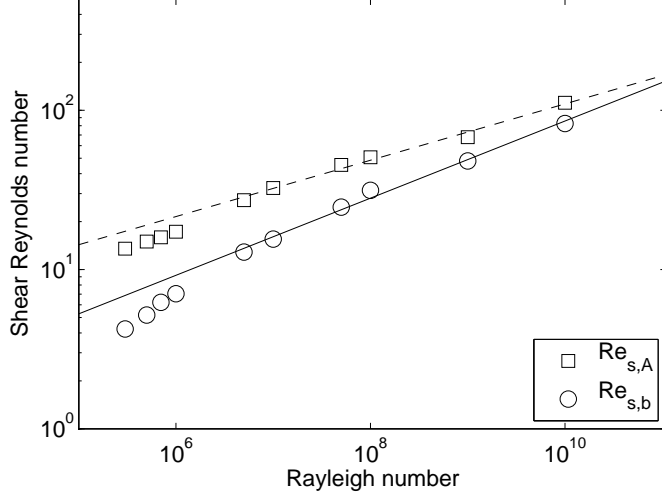


FIGURE 10. Scaling of shear Reynolds number with Rayleigh number. The corresponding power law fits to the first six data points are $Re_{s,A} = (1.9 \pm 0.6)Ra^{0.18 \pm 0.01}$ (dashed line) and $Re_{s,b} = (0.3 \pm 0.1)Ra^{0.24 \pm 0.01}$ (solid line). The shear Reynolds numbers are determined in correspondence with Eqn. (4.3).

4.3. Local boundary layer scales for different aspect ratios

The analysis has been discussed so far for a cell with unity aspect ratio. In this case the large-scale circulation consists of a single roll. The question which we want to investigate in the following is if the boundary layer analysis is sensitive to the multi-roll circulation patterns that appear in larger aspect ratio systems (see Bailon-Cuba *et al.* (2010) for a detailed discussion of the evolving large-scale patterns as a function of the aspect ratio). We conducted a DNS at an aspect ratio $\Gamma = 3$ for a Rayleigh number $Ra = 10^8$. In this setting two large circulation rolls co-exist. Figure 11 compares the time-averaged temperature and horizontal velocity fields for $\Gamma = 1$ and 3. We have averaged over 39 free-fall times for $\Gamma = 3$, short enough that the pattern has not evolved/drifted significantly enough to smear out the large-scale flow. For $\Gamma = 1$, we took this average over 104 free-fall times. Both time intervals are too short to capture the very slow dynamics of the large-scale circulation (Shi *et al.* (2012)). This would require significantly longer run times which we cannot perform for these fine grids. Therefore the mean flow which we display in both panels is quasi static to a very good approximation. Clearly observable is the fingerprint of the single circulation roll in the top panel of the figure. This circulation which is downwelling at the bottom of the panel and upwelling at the top of the panel is in line with slight mean temperature differences across the plane which are taken at $z = \delta_T/2$. The colder spot of averaged temperature (brown) is connected with the downwelling toward the bottom plate, the warmer spot (yellow) with the upwelling from the bottom plate.

The mean flow pattern is more complex in the case of the larger aspect ratio. Near the center we observe a pronounced convergence zone where the circulation flow is upwelling. Colder spots of downwelling mean circulation are distributed close to the side walls. In a streamline plot (not shown) of the time-averaged velocity field one observes two circulation rolls. The boundary analysis for this cell is conducted either across the whole plane as before or it is localized in two windows which are added to the lower panel of

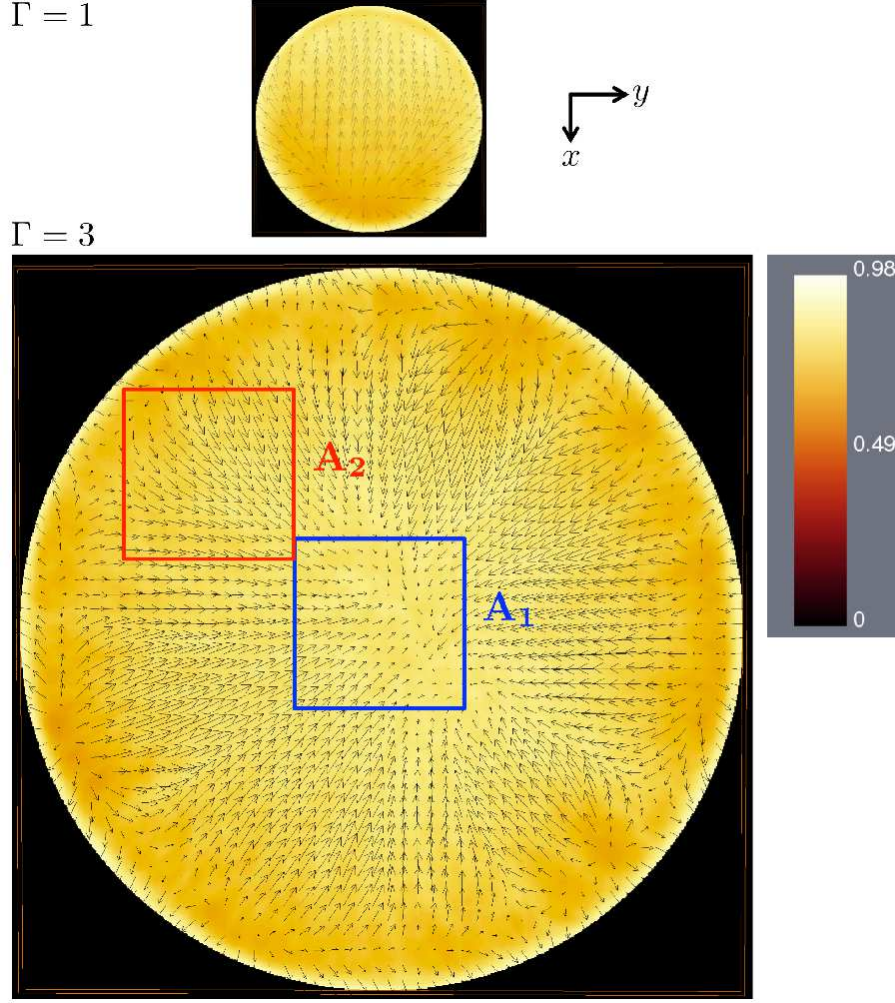


FIGURE 11. Time averaged velocity and temperature field for the simulation runs at $Ra = 10^8$. Top figure is for $\Gamma = 1$, the bottom figure is for $\Gamma = 3$. We display a contour plot of the time-averaged temperature field at $z = \delta_T/2$ in combination with the time-averaged velocity field at $z = 2\delta_T$. Vectors are a projection into the x - y plane. The sub areas A_1 and A_2 are used for a local analysis of the local boundary layer scales. Area A_1 is chosen at the interface between two large-scale circulation rolls while A_2 is inside one of the two large-scale circulation rolls. Both cases are a view from the top onto the bottom region of the convection cell. All thickness scales are measured in units of H .

Fig. 11. Window A_1 ($-0.35 < x, y < 0.35$) is put right into the convergence zone with dominantly upward motion while window A_2 ($-1.05 < x < -0.35$ and $-1.00 < y < -0.30$) corresponds with the situation as being present in the case of $\Gamma = 1$.

In Fig. 12 we compare different PDFs for two different aspect ratios. Since the Rayleigh number is the same for the two different aspect ratios we chose here to not scale the boundary layer thicknesses by their corresponding mean values. The mean boundary layer thicknesses are given in Table 3 for comparison and we see that the mean values for all boundary layer thicknesses are smaller in the $\Gamma = 1$ cell than for the whole $\Gamma = 3$ cell. This is particularly true for the outer velocity boundary layer thickness which can be explained in part by the larger u_{rms} prefactor for the $\Gamma = 3$ cell (see Table 1). The other

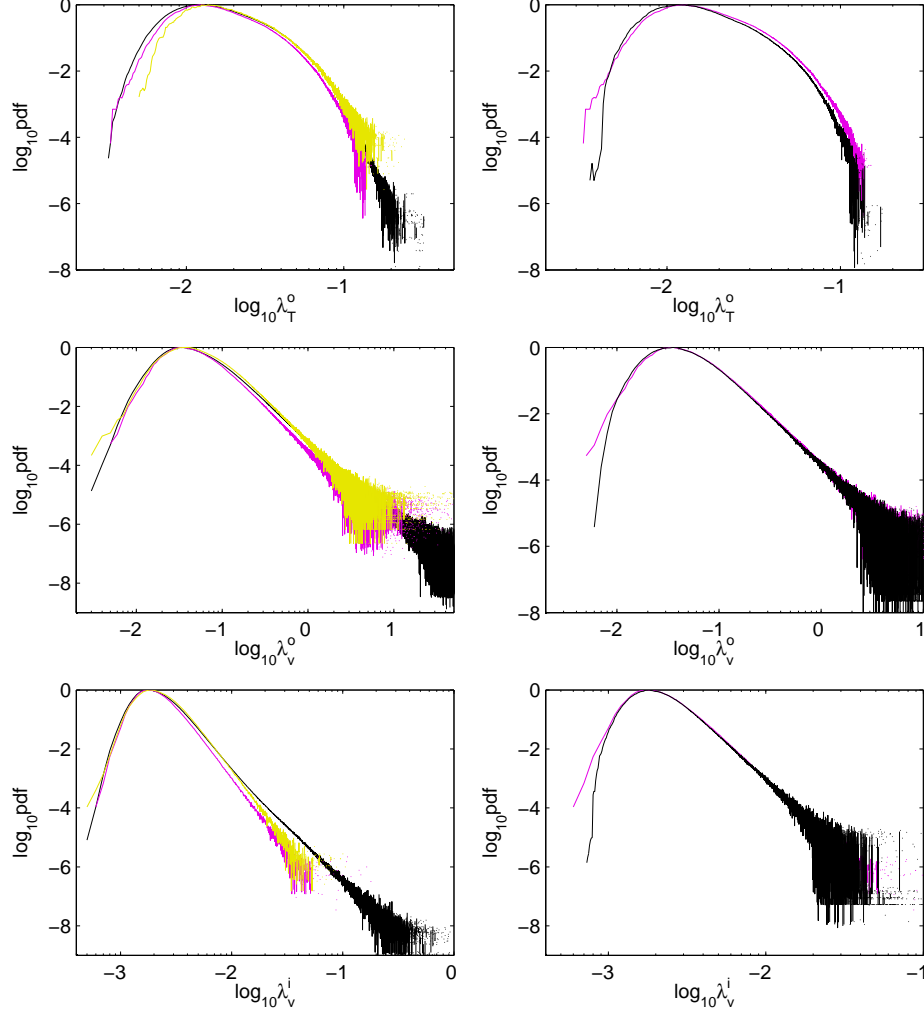


FIGURE 12. A comparison of the PDFs of the local boundary layer methods for two different aspect ratios, (both at a Rayleigh number of 1×10^8). The left panel compares the PDFs taken over the sub areas to PDFs of the entire cell all for $\Gamma = 3$ where: black is for the entire cross-sectional area, yellow (light gray) is A_1 and purple (dark gray) is A_2 , where the sub areas are defined in Figure 11. The right panel compares the PDFs taken over the sub area A_2 to PDFs of the bulk for $\Gamma = 1$ where: purple (dark gray) is $\Gamma = 3, A_2$ and black is $\Gamma = 1$, bulk ($r < 0.3$). All thickness scales are measured in units of H .

discrepancies can be explained by the different flow geometries, and when the average is taken over subvolume A_2 , the $\Gamma = 3$ data agrees best with the $\Gamma = 1$ case as would be expected.

In the left column of Fig. 12, data for $\Gamma = 3$ taken over different areas are compared. Note that the local outer boundary layer thicknesses are larger than H in some cases. This is for the same reason as in Figure 3 and we again present the data unscaled here. The distribution of λ_T^o taken over A_2 shows the sparsest tail. The right tail of the PDF taken

Area Range	$\langle \lambda_T^o \rangle$	$\langle \lambda_v^o \rangle$	$\langle \lambda_v^i \rangle$
$\Gamma = 1, r < 0.3$	0.0193 ± 0.0001	0.0139 ± 0.0002	0.00238 ± 0.00001
$\Gamma = 3$, whole plate	0.0214 ± 0.0001	0.0197 ± 0.0002	0.00251 ± 0.00001
$\Gamma = 3, A_1$	0.0204 ± 0.0001	0.0193 ± 0.0003	0.00257 ± 0.00001
$\Gamma = 3, A_2$	0.0207 ± 0.0001	0.0160 ± 0.0002	0.00236 ± 0.00001

TABLE 3. Mean values of the various boundary layer thicknesses for different aspect ratios and different regions. The corresponding PDFs are plotted in Fig. 12.

over the convergence zone A_1 is slightly fatter as larger thermal plumes will prominently rise here and enhance the local thermal boundary layer scale. The PDF obtained for the whole cell falls consistently in between which indicates that side wall effects become increasingly subdominant. The local analysis is almost insensitive with respect to the outer velocity scale, λ_v^o . The right tail of the data obtained over A_2 is slightly sparser. For the inner scale, λ_v^i , data obtained over A_1 and A_2 almost coincide. Here, we observe a fatter tail for the analysis across the whole area. This circumstance might display the impact of recirculation zones at the side walls for which local wall shear stresses can change sign and therefore contribute to larger local scale events.

In the right column of the same figure, the results obtained for $\Gamma = 1$ in the bulk with $\Gamma = 3$ for A_2 are compared. At a first glance, the PDFs of both data records coincide quite well in all three cases for the majority of amplitudes. We observe in all cases a more pronounced left and right tail for the larger aspect ratio (except for λ_v^i where the right tails almost coincide). Finer local scales imply steeper local gradients and vice versa. These gradients can be established since the dynamics in the convective turbulence is less constrained by cell geometry such that, e.g., the fluid can be swept over longer distances. Turning back to Fig. 11, it can be seen that the area A_2 with a nearly uniform mean flow is almost as large as the whole area in the top panel of the same figure. Our conjecture might also be supported by the fact that the velocity fluctuations are larger in the case of $\Gamma = 3$ compared to $\Gamma = 1$ at the same Rayleigh number of $Ra = 10^8$, as documented in Tab. 1. In summary, our analysis confirms that the results of the local boundary layer scale analysis is somewhat dependent on the geometry, mainly for the tail events which are associated with very fine or very coarse local scales.

4.4. Dissipation layer thickness analysis

Following Petschel *et al.* (2013), we compute the velocity and thermal dissipation layer thicknesses from (1.3). As already mentioned in the introduction, we will denote the kinetic energy dissipation layer thickness as d_v and the thermal dissipation layer thickness as d_T . While Petschel *et al.* kept the Rayleigh number at a moderate value of $Ra = 5 \times 10^6$ and varied the Prandtl number over a very wide range ($0.01 \leq Pr \leq 300$), we will use our data to study the dissipation scales as a function of Rayleigh number. We show representative examples of dissipation layer thickness calculations in Fig. 13. In the left panel, the plane-time averaged thermal dissipation profiles (solid lines) and the corresponding volume mean values (dashed lines) are displayed. The same is repeated for the kinetic energy dissipation rate in the right panel. We observe a systematic trend in the case of d_T . The mean thermal energy dissipation rate decreases and the intersection point with the vertical profile is shifted in proportion towards the wall indicating an increasingly finer thermal dissipation layer thickness d_T .

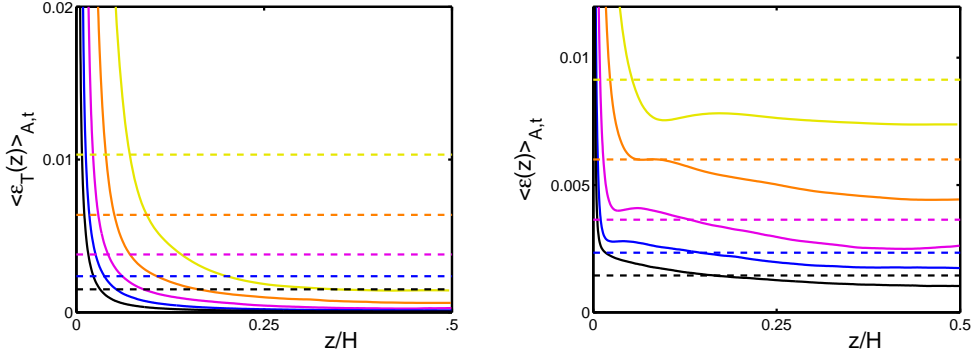


FIGURE 13. Horizontally averaged dissipation rates (solid lines) for various Rayleigh numbers. The left panel is for $\langle \epsilon_T(z) \rangle_{A,t}$ and the right panel is for $\langle \epsilon(z) \rangle_{A,t}$. The profiles were also averaged about $z/H = 0.5$ so that the top and bottom half both contribute to the profile. The dashed lines give the volume averaged dissipation rate $\langle \epsilon_T \rangle_{V,t}$ (left) and $\langle \epsilon \rangle_{V,t}$ (right). The intersection of these two lines gives the dissipation layer thickness d_T and d_v , respectively. The range of Rayleigh number is given in Fig. 3 and the parameters are the same.

The situation is different in the case of the kinetic energy dissipation layer thickness. Again, the mean energy dissipation decreases with increasing Rayleigh number. However the mean vertical profile changes: in particular the dissipation starts to decrease monotonically towards the mid plane for the higher Rayleigh numbers. This causes a jump in the intersection point which becomes visible in Fig. 14. This figure shows the dissipation layer thickness data for all of the Rayleigh numbers we used in our study. We observe a change in the scaling at $Ra \sim 10^7$ for both the thermal and the kinetic dissipation layer thicknesses. While the thermal dissipation layer thickness changes from a power law exponent of -0.17 for the first six data points to -0.07 for the last five data points, the kinetic energy dissipation layer thickness remains almost constant (we fit an exponent of -0.03 to the first six data points) initially and increases afterwards non-monotonically. As a guide to the eye we added the classical thickness data of δ_T and δ_v to Fig. 14 as gray lines and symbols.

At this point we can only speculate about the reasons for a change in the trend with Ra , in particular for the kinetic energy dissipation layer thickness. We conjecture that this transition is related to a transition observed by Schumacher *et al.* (2014). They found that the scaling of the moments of the kinetic energy dissipation rate (defined in Eq. (2.9)) with Reynolds number follow universal power laws for sufficiently high Reynolds numbers. Hence, beyond the transitional Reynolds number, small-scale turbulence in the bulk obeys the properties of a fully developed turbulent state. For Rayleigh-Bénard convection this transition occurs at a Reynolds number corresponding to $Ra \simeq 5 \times 10^6$. Table 1 indicates that the rms values of the velocity field \mathbf{u} remain at about the same level up to a Rayleigh number of 10^7 and start to decrease slowly but monotonically with increasing Rayleigh number. The mean energy dissipation is found to follow a power law of $\langle \epsilon \rangle_{V,t} = (0.13 \pm 0.02) \times Ra^{-0.19 \pm 0.01}$ which is also consistent with the scaling reported in Scheel *et al.* (2013), obtained there over a smaller range of Rayleigh numbers than in the present work. The decrease of the velocity fluctuations can be related to a reduced coherence of the detaching thermal plumes. Consequently the mean vertical dissipation profiles will vary because strong shear layers due to rising or falling plumes becomes less pronounced. Our simulation data suggest that both dissipation layer thickness scales pass through a transition in their Rayleigh number dependence.

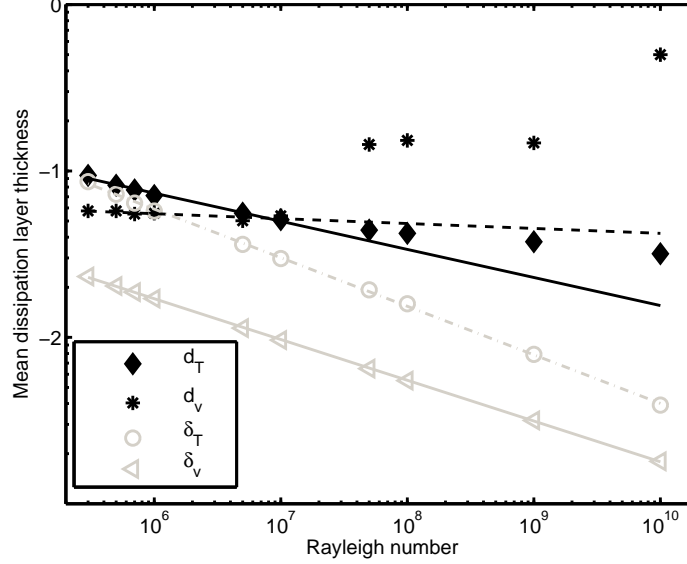


FIGURE 14. Scaling of thermal and velocity dissipation layers with Rayleigh number. The black solid diamonds are for d_T , and the fit to the first six data points (solid black line) is $d_T = (0.8 \pm 0.2)Ra^{-0.17 \pm 0.01}$. The black stars are for d_v , and the fit to the first six data points (dashed line) is $d_v = (0.08 \pm 0.02)Ra^{-0.03 \pm 0.01}$. Note the interesting transition for the dissipation layer thicknesses for $1 \times 10^7 < Ra < 1 \times 10^8$. The classical boundary layer thicknesses and their corresponding fits are given by the grey symbols and lines (same data as in Figures 8 and 9).

4.5. Friction coefficient

A further interesting question which is related to the discussion in the last subsection is how the friction coefficient behaves in the convection system. We define here the dimensionless friction coefficient as

$$c_\epsilon = \frac{\langle \epsilon \rangle_{V,t}}{u_{rms}^3}. \quad (4.4)$$

Figure 15 shows the friction coefficient as a function of the Rayleigh number which can be fitted by a power law with an exponent of -0.16. We have added the slopes which would follow from a laminar flow, $c_\epsilon \sim Re^{-1} \sim Ra^{-1/2}$, and a fully turbulent wall bounded flow, $c_\epsilon \sim Re^{-1/4} \sim Ra^{-1/8}$ (at moderate Reynolds numbers), given the simple Re - Ra scaling of $Re \sim \sqrt{Ra}$ which is almost satisfied for our data as mentioned in Section 2. Our detected slope is also consistent with the first data points of Fig. 16(a) in Verzicco & Camussi (2003) (denoted as the surrogate friction coefficient therein). If we compare to experiments for water, $\Gamma = 1$ and Rayleigh numbers overlapping with ours, our exponent disagrees with Sun *et al.* (2008) who measured an exponent of -0.28 (their experiment was in an elongated rectangular box) but agrees with Wei & Xia (2013) who measured an exponent of -0.19 ± 0.02 (their experiment was in a cylindrical container).

The behavior of the friction coefficient indicates that the boundary layer dynamics, in which the major part of the kinetic energy is dissipated, is a mixture of laminar phases interrupted by bursts due to rising plumes and local vortices, i.e., elements which are characteristic of a turbulent boundary layer. This has also been found experimentally by du Puits *et al.* (2014) and also numerically by Shi *et al.* (2012), who performed a detailed analysis of the dynamics in the vicinity of the heating plate.

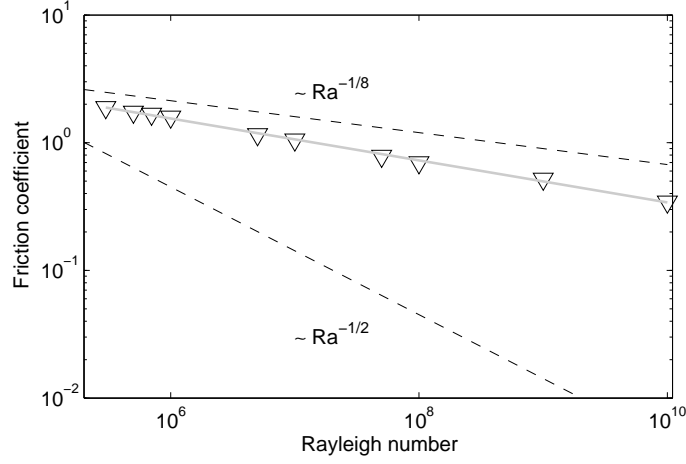


FIGURE 15. Friction coefficient c_ϵ as a function of the Rayleigh number. As a guide to the eye we add the scaling which for a purely laminar flow is $c_\epsilon \sim Ra^{-1/2}$, and for a fully developed turbulent wall-bounded flow is $c_\epsilon \sim Ra^{-1/8}$ (dashed black lines). These scalings would follow when the Reynolds number is related to the Rayleigh number by $Re \sim \sqrt{Ra}$. The fit to the simulation data gives $c_\epsilon = (15.0 \pm 1.4) \times Ra^{-0.16 \pm 0.01}$ and is indicated by a solid gray line.

Another perspective is provided by Chong *et al.* (2012) who found critical points (i.e. nodes/foci) in the wall shear stress vector field in a turbulent channel flow simulations. Similar patterns have been reported in Grosse & Schröder (2009) for an experimental determination of the wall-stress vector field with micro-pillars in a duct flow. These critical points were rare, but did exist and they postulated that these critical points would give rise to a generation of turbulence at the wall. We also find such critical points in our simulations as seen in Figure 16 where we have plotted the wall shear stress vector field lines superimposed on a color density plot of the magnitude of τ_w for a Rayleigh number of 1×10^7 and $\Gamma = 1$. The white areas contain exactly those zero points of the vector field that have been excluded in our velocity boundary layer scale analysis. Their role for the enstrophy production will be discussed in a subsequent work.

5. Summary and outlook

This paper presented a boundary layer analysis in turbulent Rayleigh-Bénard convection. The motivation for this work is threefold.

First, we wish to generalize the boundary layer analysis to a fully local approach. This perspective best captures the spatio-temporal variations and the transitional character of the boundary layer dynamics in which quasi-laminar sequences are interrupted by bursts and vortex formation processes which are partly connected to the detachment of plumes.

Second, the local definition is to our view necessary since the near-wall boundary layer dynamics is highly inhomogeneous across the bottom and top plates in closed convection cells which are the standard experimental setup. Recall that a well-defined mean flow as in a pipe or channel is absent here. The large-scale circulation itself is a complex three-dimensional time-dependent structure filling the whole cell. We demonstrate this circumstance for example by a comparison of runs at the same Ra and Pr , but different aspect ratio. It matters where the data are taken: away from the side walls, in the middle of the cell or in between a multi-roll large-scale circulation configuration which can build

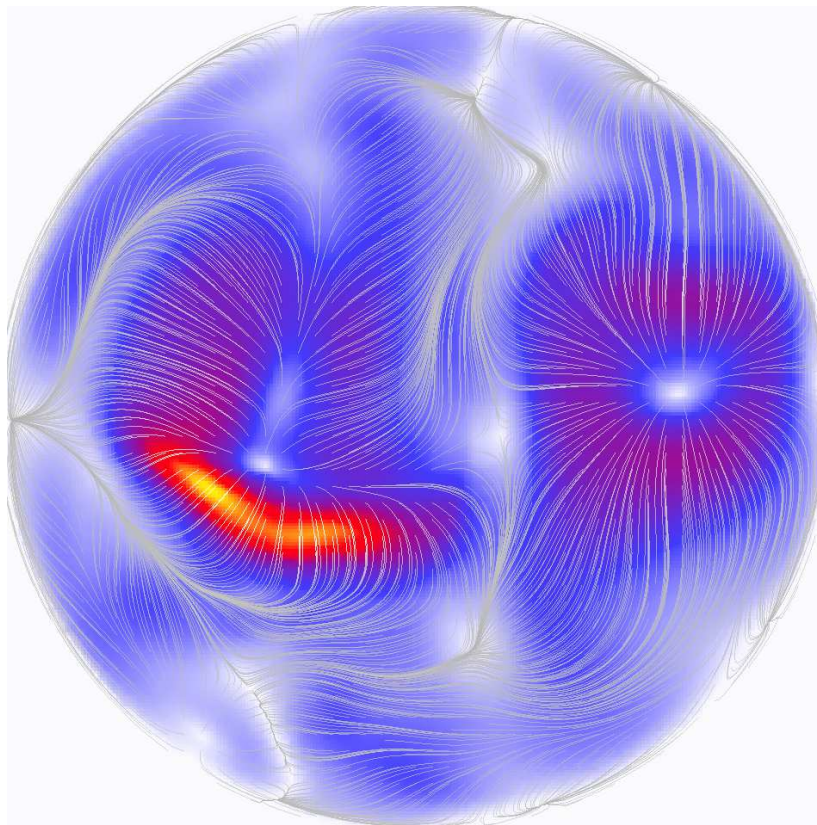


FIGURE 16. Color density plot of the instantaneous magnitude of τ_w (calculated from the magnitude of (3.4)) along with the gray field lines of the wall shear stress vector field $(\frac{du}{dz}, \frac{dv}{dz})$ at the bottom plate for $Ra = 1 \times 10^7, \Gamma = 1.0$. Color coding is as follows. White is the minimum and yellow denotes maximum magnitude.

up in cells with aspect ratios $\Gamma > 1$. In each of these cases the tails of the local boundary layer scale distributions are found to differ slightly, hence prefactors and scaling exponents in power laws for the first moments derived from the distributions will vary. The study also complements previous experimental and numerical local boundary layer analyses. It confirms the inhomogeneous character of the dynamics and resulting statistics which is found to depend on the location at the plate.

Third, our analysis makes also the first contact to recent efforts to study local dissipation scales and higher order statistics of velocity gradients in bulk turbulence of several turbulent flows. The distribution of the local boundary layer scales is thus a direct manifestation of the strong spatial intermittency of the gradients in the boundary layer.

With this fully local boundary layer analysis, we are able to assemble good statistics on the distribution of boundary layer thicknesses. We find that the overall shape of the PDFs for both inner and outer and thermal and velocity boundary layer thicknesses take on a universal shape, but one which is not lognormal. The scaling exponents of the mean (first moment) outer boundary layer thicknesses agree well with previous results obtained from the more traditional slope method, when similar plate averagings are compared. However, the mean inner velocity boundary layer thicknesses tend to scale more steeply. We also are able to compute a shear Reynolds number from our data and find that our scaling exponent for the bulk-averaged method ($Re_{s,b} \propto Re^{0.24 \pm 0.01}$)

agrees with other results ($Re_s \propto Ra^{0.267 \pm 0.0386}$). We also computed dissipation layer thicknesses and found a transition in both thickness scalings with Rayleigh number at around $1 \times 10^7 < Ra < 1 \times 10^8$, exactly where a transition to small-scale turbulence in the bulk is expected from Schumacher *et al.* (2014). Finally our friction coefficient scaling with Rayleigh number ($c_\epsilon \propto Ra^{-0.16 \pm 0.01}$) suggests that the boundary layer is in a transitional regime.

The present study can be a first step only. A formal conclusion on the transitional behavior of the boundary layer requires data at larger Rayleigh numbers and larger aspect ratios as well. A further aspect to study is the Prandtl number dependence. This would also help to better understand the parameter dependence of the dissipation layers in comparison to the other scales. In the present study the thermal and velocity boundary layers are similar in size since the Prandtl number is close to one, but for Prandtl numbers both larger and smaller than one the boundary layer thicknesses will differ. In particular for very low Prandtl numbers, we can expect dramatic changes in the boundary layer dynamics and the related turbulence production mechanisms based on our current efforts in this direction which will be discussed elsewhere.

This work was supported by the Deutsche Forschungsgemeinschaft within Research Unit 1182. Supercomputing time for the majority of the present RBC simulations has been provided on BG/Q JUQUEEN by the Jülich Supercomputing Centre (Germany) within the Large-Scale Project HIL07 of the German Gauss Centre for Supercomputing. The simulation run for the larger-aspect ratio cell ($\Gamma = 3$) was made possible by the PRACE Initiative. We acknowledge that the results of this research have been achieved using the PRACE-2IP project (FP7 RI-283493) resource BG/Q Hartree based in UK at Daresbury Laboratory. Both of us wish to thank also Paul Fischer for his initial help with the Nek5000 spectral element code package and Bruno Eckhardt for discussions.

REFERENCES

- AHLERS, G., GROSSMANN, S. & LOHSE, D. 2009 Heat transfer & large-scale dynamics in turbulent Rayleigh-Bénard convection. *Rev. Mod. Phys.* **81**, 503–537.
- BAILON-CUBA, J., EMRAN, M. S. & SCHUMACHER, J. 2010 Aspect ratio dependence of heat transfer and large-scale flow in turbulent convection. *J. Fluid Mech.* **655**, 152–173.
- BELMONTE, A., TILGNER, A. & LIBCHABER, A. 1994 Temperature and velocity boundary layers in turbulent convection *Phys. Rev. E* **50**, 269–279.
- BLASIUS, H. 1908 Grenzschichten in Flüssigkeiten mit kleiner Reibung, *Z. Math. Physik* **56**, 1–37.
- CHILLÀ, F. & SCHUMACHER, J. 2012 New perspectives in turbulent Rayleigh-Bénard convection. *Eur. J. Phys.* **35**, 58 (25 pages).
- CHONG, M. S., MONTY, J. P., CHIN, C. & MARUSIC, I. 2012 The topology of skin friction and surface vorticity fields in wall-bounded flows. *Journal of Turbulence* **13**, No. 6, 1–10.
- DEVILLE, M. O., FISCHER, P. F. & MUND, E. H. 2002 *High-order methods for incompressible fluid flow* Cambridge University Press.
- DU PUIITS, R., RESAGK, C. & TRESS, A. 2007a Mean velocity profile in confined turbulent convection. *Phys. Rev. Lett.* **99**, 234504 (4 pages).
- DU PUIITS, R., RESAGK, C., TILGNER, C., BUSSE, F. H. & TRESS, A. 2007b Structure of thermal boundary layers in turbulent Rayleigh-Bénard convection. *J. Fluid Mech.* **572**, 231–254.
- DU PUIITS, R., RESAGK, C. & TRESS, A. 2010 Measurements of the instantaneous local heat flux in turbulent Rayleigh-Bénard convection. *New J. Phys.* **12**, 075023 (13 pages).
- DU PUIITS, R., LI, L., RESAGK, TRESS, A. & WILLERT, C. 2014 Turbulent boundary layer in high Rayleigh number convection in air. *Phys. Rev. Lett.* **112**, 124301 (4 pages).

- FISCHER, P. F. 1997 An overlapping Schwarz Method for spectral element solution of the incompressible Navier-Stokes equations. *J. Comp. Phys.* **133** 84–101.
- GROSSE, S. & SCHRÖDER, W. 2009 Wall-shear stress patterns of coherent structures in turbulent duct flow. *J. Fluid Mech.* **633**, 147–158.
- GROSSMANN, S. & LOHSE, D. 2000 Scaling in thermal convection: a unifying theory. *J. Fluid Mech.* **407**, 27–56.
- GRÖTZBACH, G. 1983 Spatial resolution requirements for direct numerical simulation of the Rayleigh-Bénard convection. *J. Comput. Phys.* **49**, 241–269.
- HAMLINGTON, P. E., KRASNOV, D., BOECK, T. & SCHUMACHER, J. 2012 Local dissipation scales and energy dissipation-rate moments in channel flow. *J. Fluid Mech.* **701** 419–429.
- HARTLEP, T., TILGNER, A. & BUSSE, F. H. 2005 Transition to turbulent convection in a fluid layer heated from below at moderate aspect ratio. *J. Fluid Mech.* **554** 309–322.
- HE, X., FUNFSCHILLING, D., NOBACH, H., BODENSCHATZ, E. & AHLERS, G. 2012 Transition to the ultimate state of turbulent Rayleigh-Bénard convection. *Phys. Rev. Lett.* **108** 024502 (4 pages).
- KAISER, R. & DU PUIITS, R. 2014 Local wall heat flux in confined thermal convection. *Int. J. Heat Mass Trans.* **73**, 752–760.
- LI, L. SHI, N., DU PUIITS, R., RESAGK, C., SCHUMACHER, J. & THESS, A. 2012 Boundary layer analysis in turbulent Rayleigh-Bénard convection in air: Experiment versus simulation. *Phys. Rev. E* **86**, 026315 (12 pages).
- LUI S.-L. & XIA, K.-Q. 1998 Spatial structure of the thermal boundary layer in turbulent convection *Phys. Rev. E* **57**, 5494–5503.
- PETSCHER, K., STELLMACH, S., WILCZEK, M., LÜLFF, J. & HANSEN, U. 2013 Dissipation layers in Rayleigh-Bénard convection: A unifying view. *Phys. Rev. Lett.* **110**, 114502 (4 pages).
- POHLHAUSEN, E. 1921 Der Wärmetausch zwischen festen Körpern und Flüssigkeiten mit kleiner Reibung und kleiner Wärmeleitung. *Z. Angew. Math. Mech.* **1**, 115–121.
- POPE, S. B. 2000 *Turbulent flows*, Cambridge University Press.
- PRANDTL, L. 1905 Über Flüssigkeitsbewegung bei sehr kleiner Reibung. Proceedings of the III. International Mathematicians Congress, Heidelberg, 1904. B. G. Teubner, Leipzig, 1905, 484–491.
- QIU, X.-L., & XIA, K.-Q. 1998 Spatial structure of the viscous boundary layer in turbulent convection *Phys. Rev. E* **58**, 5816–5820.
- SCHEEL, J. D., KIM, E. & WHITE, K. R. 2012 Thermal and viscous boundary layers in turbulent Rayleigh-Bénard convection. *J. Fluid Mech.* **711**, 281–305.
- SCHEEL, J. D., EMRAN, M. S. & SCHUMACHER, J. 2013 Resolving the fine-scale structure in turbulent Rayleigh-Bénard convection. *New J. Phys.* **15**, 113063 (32 pages).
- SCHUMACHER, J., YEUNG, P.K. & SREENIVASAN, K. R. 2005 Very fine structures in scalar mixing. *J. Fluid Mech.* **531**, 113–122.
- SCHUMACHER, J. 2007 Sub-Kolmogorov scale fluctuations in fluid turbulence. *Europhys. Lett.* **80**, 54001 (6 pages).
- SCHUMACHER, J., SCHEEL, J. D., KRASNOV, D., DONZIS, D. A., YAKHOT, V., & SREENIVASAN, K. R. 2014 Small-scale universality in fluid turbulence. *Proc. Nat. Acad. Sci. USA* **111**, 10961–10965.
- SHI, N., EMRAN, M. S. & SCHUMACHER, J. 2012 Boundary layer structure in turbulent Rayleigh-Bénard convection. *J. Fluid Mech.* **706**, 5–33.
- SHISHKINA, O., STEVENS, R. A. J. M., GROSSMANN, S. & LOHSE, D. 2010 Boundary layer structure in turbulent thermal convection and its consequences for the required numerical resolution. *New J. Phys.* **12**, 075022 (17 pages).
- SIGGIA, E. D. 1994 High Rayleigh number convection. *Annu. Rev. Fluid Mech.* **26**, 137–168.
- SUN, C., CHEUNG, Y.-H. & XIA, K.-Q. 2008 Experimental studies of the viscous boundary layer properties in turbulent Rayleigh-Bénard convection. *J. Fluid Mech.* **605**, 79–113.
- STEVENS, R. J. A. M., VERZICCO, R. & LOHSE, D. 2010 Radial boundary layer structure in Rayleigh-Bénard convection. *J. Fluid Mech.* **643**, 495–507.
- STEVENS, R. J. A. M., VERZICCO, R. & LOHSE, D. 2012 Thermal boundary layer profiles in turbulent Rayleigh-Bénard convection in a cylindrical sample. *Phys. Rev. E* **85**, 027301 (5 pages).

- TROMPERT R. & HANSEN, U. 1998 Mantle convection simulations with rheologies that generate plate-like behaviour. *Nature* **395**, 686–689.
- URBAN, P., HANZELKA, P., KRALIK, T., MUSILOVA, V., SRNKA, A. & SKREBK, L. 2012 Effect of boundary layers asymmetry on heat transfer efficiency in turbulent Rayleigh-Bénard convection at very high Rayleigh numbers. *Phys. Rev. Lett.* **109**, 154301 (4 pages).
- VAN REEUWIJK, M., JONKER, H. J. J. & HANJALIĆ, K. 2008b Wind and boundary layers in Rayleigh-Bénard convection. II. Boundary layer character and scaling. *Phys. Rev. E* **77**, 036312 (10 pages).
- WAGNER, S., SHISHKINA, O. & WAGNER, C. 2012 Boundary layers and wind in cylindrical Rayleigh-Bénard cells. *J. Fluid Mech.* **697**, 336–366.
- VERZICCO, R. & CAMUSSI, R. 1999 Prandtl number effects in convective turbulence *J. Fluid Mech.* **383**, 55–73.
- VERZICCO, R. & CAMUSSI, R. 2003 Numerical experiments on strongly turbulent thermal convection in a slender cylindrical cell. *J. Fluid Mech.* **477**, 19–49.
- WEI, P. & XIA, K.-Q. 2013 Viscous boundary layer properties in turbulent thermal convection in a cylindrical cell: the effect of cell tilting *J. Fluid Mech.* **720**, 140–168.
- ZHOU, Q., STEVENS, R. J. A. M., SUGIYAMA, K., GROSSMANN, S., LOHSE, D. & ZIA, K.-Q. 2010 Radial boundary layer structure in Rayleigh-Bénard convection. *J. Fluid Mech.* **643**, 495–507.
- ZHOU, Q. & XIA, K.-Q. 2010 Measured instantaneous viscous boundary layer in turbulent Rayleigh-Bénard convection. *Phys. Rev. Lett.* **104**, 104301 (4 pages).
- ZHOU & XIA, K.-Q. 2010a Universality of local dissipation scales in buoyancy-driven turbulence. *Phys. Rev. Lett.* **104**, 124301 (4 pages).
- ZHOU, Q., SUGIYAMA, K., STEVENS, R. J. A. M., GROSSMANN, S., LOHSE, D. & ZIA, K.-Q. 2011 Horizontal structures of velocity and temperature boundary layers in two-dimensional numerical turbulent Rayleigh-Bénard convection. *Phys. Fluids* **23**, 125104.